2015

Mid-infrared Plasmonics

Farnood Khalilzadeh Rezaie
University of Central Florida

University of
Central
Florida

STARS
Showcase of Text, Archives, Research & Scholarship

MID-INFRARED PLASMONICS

by

FARNOOD KHALILZADEH REZAIE
B.S., University of Tehran, 2009
M.S., University of Central Florida, 2011

A dissertation submitted in partial fulfillments of the requirements
for the degree of Doctor of Philosophy
in the Department of Physics
in the College of Sciences
at the University of Central Florida
Orlando, Florida

Summer Term
2015

Major Professor: Robert E. Peale

ABSTRACT

This dissertation reports investigations into materials for, and applications of, infrared surface plasmon polaritons (SPP). SPPs are inhomogeneous electromagnetic waves that are bound to the surface of a conductor. Tight confinement of electromagnetic energy, the primary virtue of SPPs for so-called "plasmonic" applications, requires plasma frequencies for the conductor near the intended infrared operational frequencies. This requires carrier concentrations that are much less than those of usual metals such as gold and silver. I have investigated the optical properties and SPP excitation resonances of two materials having infrared plasma frequencies, namely the semimetal bismuth and the transparent conducting fluorine-doped tin-oxide (FTO). The complex permittivity spectra for evaporated films of Bi were found to be distinctly different than earlier reports for crystal or polycrystalline films, and SPP excitation resonances on Bi-coated gratings were found to be disappointingly broad. Permittivity spectra for chemical spray deposited FTO were obtained to long-wave IR wavelengths for the first time, and nano-crystalline FTO-coated silicon lamellar gratings show remarkable conformity. SPP excitation resonances for FTO are more promising than for Bi. Thus, FTO appears to be a promising SPP host for infrared plasmonics, e.g. a planer waveguide plasmonic spectral sensor, whose design was elaborated and investigated as part of my research and which requires SPP-host coating on deep vertical side walls of a trench-like analyte interaction region. Additionally, FTO may serve as a useful conducting oxide for a near-IR plasmonic spectral imager that I have investigated theoretically.

To my family.

"Research is what I'm doing, when I don't know what I'm doing."

Werhner von Braun

ACKNOWLDEGMENT

TABLE OF CONTENTS

LIST OF FIGURES

CHAPTER ONE: INTRODUCTION

Surface plasmon polaritons (SPPs) are collected electron oscillations of surface charge density that propagate along dielectric/metal interface. The first experimental observation of SPPs on metals were reported in early 20th century by Wood [1]. Dark and light bands in the reflection spectrum of metallic gratings were observed when transverse magnetic light (TM) hits the metallic gratings. This uneven distribution of light and dark bands were not predicted and explained by theory of diffraction gratings and that is why they were called "Woods anomalies". The first theoretical work on these so called Woods anomalies was published in 1907 by Lord Rayleigh [2].

Rayleigh's formalism predicted wavelengths (Rayleigh's wavelength) in which the scattered field is singular and also coincides with Wood's anomalies wavelengths. This singularity in the scattered field was predicted by Rayleigh and a resonant type anomaly due to guided waves. In 1941, Fano [3] connected earlier theoretical work of Sommerfeld and Zenneck on radio waves propagating along the surface of a conductor to explain the experimental results of Wood and Rayleigh.

Pine and Bohm in 1956 [4] introduced these electrons on metal as plasma which later in 1958 inspired Ritchie [5] to name them as "Plasmons". In following years, Otto [6] and Kretschmann-Raethers [7] used the total internal reflection (TIR) phenomena in a high-index prism near a metal interface to excite surface plasmons. This work focuses on optical exciton of SPPs by grating and prism couplers. Optical excitation of SPPs by prisms is well understood while complicated numerical algorithms based on scattering matrix analysis [8, 9] are being used to describe coupling of SPPs.

Surface plasmon polaritons are used in variety of optoelectronic applications which range from biosensing, solar cells, metamaterials and even cancer treatment [10]. SPPs are the primary means of energy and information transport in the blossoming field of nano-photonics. Thus, nano-photonic devices based on them are popularly referred to as "plasmonics". Figure 1 represents a historical timeline of development in SPPs which are related to this dissertation. More comprehensive of surface plasmon polaritons and plasmonics can be found in [11, 12].
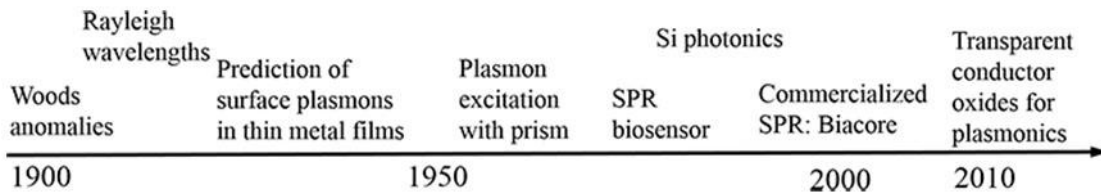
Figure 1 Timeline of breakthroughs in plasmonics.

Despite extensive worldwide research and development in plasmonics [4], the only practical commercial devices based on SPPs are surface plasmon resonance (SPR) biosensors. These are based on the observation of photon-to-plasmon coupling resonances that change when bimolecular analytes selectively bind to biological recognition elements (BRE) on a functionalized conductor surface [5, 6]. Additionally, a coupling device such as a prism or grating provides momentum matching between photons and SPPs.

The first biosensor based on SPPs was developed in Sweden by Nylander and Lindberg [13, 14]. Lindberg device works based on surface plasmon resonance (SPR) reflection when the light is shun on a metal surface. The biosensor utilizes changes in SPR to analyze biomolecule interaction at the surface of a metallic film. Lot more work on SPR sensing has been carried out

2

since [15-17] with the first commercial device based on plasmonics introduced to market in 1991 by Biacore [18].

Most SPR biosensors operate in the visible to near-infrared (NIR) wavelength range, because it is here that SPPs are most tightly bound to ordinary metals such as gold, giving good mode overlap with the molecular analytes of submicron dimensions. The opportunity that we pursue in this work is infrared SPR. A hypothesized advantage is that molecules have characteristic IR vibrational absorptions, giving rise to strong molecule-specific dispersion, e.g. [7]. The associated increase in the refractive index on the long-wavelength side of the absorption bands promises to enhance the sensitivity. The specificity of the dispersion is expected to reduce false positives due to non-specific binding.

Plasmonic waveguides are also utilized to minimize the size of optical components. Most of earlier studies are focused on SPPs in visible wavelength. Plasmonics in long wave infrared (LWIR) was first introduced by Soref and Lorenzo [19] for application of silicon waveguides in the IR. Up until this point, silicon was used in the semiconductor industry to fabricate the miniaturized electrical devices but it was shown by Soref that Si can be used as efficiently in photonics. A comprehensive review of silicon photonics can be found here [20-22].

Majority of plasmonic devices are using noble metals (i.e., Au and Ag) as hosts for excitation of SPPs in the visible and IR range of EM spectrum. Although noble metals provide the required negative permittivity for subwavelength confinement, they also possess a large imaginary component of permittivity which would result in loss in plasmon propagation [12]. Nanophotonics is in need of novel plasmonic materials which allow subwavelength optical confinement and loss mitigation, simultaneously [23-25]. This is the motivation to investigate other possible materials

as plasmonic hosts, such as highly-doped semiconductors [26], semimetals [27] and doped conducting oxides [28], as alternative for noble metals.

This dissertation focuses on the use of SPPs into the infrared (IR) region of the EM spectrum which has numerous advantages in the sensing and waveguide applications. IR surface plasmons are investigated on both prism and grating couplers for various metal, semi-metals and semiconductors [27, 29, 30]. The development and characterization of fluorine-doped tin oxide thin-films and bismuth thin films are studied for device applications in plasmonics. The subsequent chapters of this dissertation are organized in the following manner:

- Chapter2: We discuss the basic theoretical foundation of surface plasmons excited via optical methods.

- Chapter3: IR optical constants of semimetal bismuth is investigated. Experimental measurements of permittivity and reflectivity of material are used to calculate the surface plasmon properties. Calculated and measured surface plasmon resonance in grating couplers are investigated. A discussion on the origin of surface polaritons in LWIR and the applications of Bi in infrared plasmonics are discussed.

- Chapter4: Streaming Process for Electrodeless Electrochemical Deposition (SPEED) is used to fabricate high-quality fluorine-doped tin oxide (FTO) thin films on hydrophilic substrates. These FTO film are highly crystalline and adhere strongly to surface and have been extensively studied by standard material characterization methods. The direct optical bandgap is spectroscopically determined while electrical properties of the FTO films are investigated and discussed.

- Chapter5: Ellipsometry and FTIR reflectance are implemented to characterize the optical properties of FTO films. A method for fabricating high-quality FTO gratings on Si

substrate has been developed and discussed and resulting grating couplers are measured in specular- and angular- reflectance setups. The IR resonances of FTO lamellar gratings are distinct and potentially useful for sensing and opto-electronic devices.

- Chapter6: A compact plasmonic device, consisting of a spectrometer-on-a-chip, featuring a plasmonic molecular interaction region was conceived, designed, modeled, and partially fabricated. Such a device, once completed, can provide a possible chip-scale chemical sensor and spectrometer compatible with complementary-metal-oxide-semiconductor (CMOS) fabrication technology.

- Chapter7: A plasmonic photocapacitor based on electronic detection of SPPs in a Kretschmann-based prism coupler has been discussed, with the angular reflectance of the structure was both measured and calculated.

- Chapter8: The dissertation has been summarized and future work is speculated.

CHAPTER TWO: INFRARED SURFACE PLASMON POLARITINS

2.1 Theory of surface plasmon polaritons

Surface plasmon polaritons are bound electromagnetic wave at the interface of a dielectric and conductor. Oscillation of surface charge density, σ is the source for electric field. A discontinuity of the normal component of the electric field at the dielectric/conductor boundary is given by:

$$E_{z1} - E_{z0} = 4\pi\sigma \tag{1}$$

where E_{z1} and E_{z0} are normal components of electric field at the interface, respectively and σ is the surface charge density at the interface. The wavefunctions of the charge density is:

$$\sigma(x,t) = \sigma_0 e^{i(k_x x - \omega t)} \tag{2}$$

where k_x is the wavevector along the boundary and σ_0 is a constant. These charged oscillation at the interface are coupled to external electric field which has both components perpendicular to the plane of propagation and parallel to it.

When the electric field is inside the plane of propagation, the EM light is called p-polarized or transverse magnetic (TM). In this case, E lies inside the xz-plane and is defined by surface normal and the propagation vector while the magnetic field is perpendicular to this plane. The SPP field at the interface of two materials decays exponentially and inside both media. The normal component of EM field can be written as:

$$E_z = E_0 e^{i(k_x x + k_z z - \omega t)} \tag{3}$$

where k_z is the projection of k vector on z- axis. k_z has a large imaginary value which makes the SPPs to decay fast on both sides of interface. Figure 2 presents the characteristics electric fields at conductor/dielectric interface. The positive and negative signs in the x and z terms are responsible for the exponential decay in all directions.
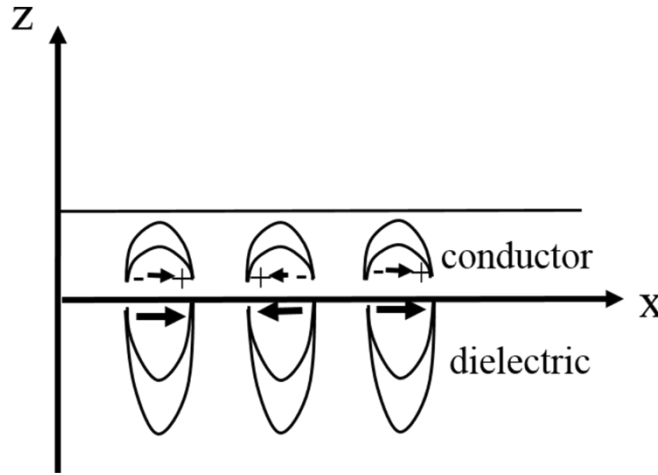
Figure 2 Characteristic electric field lines of SPPs.

x- and z-components of wave vector are related to each other according to:

$$k_x^2 + k_{zd,zc}^2 = \varepsilon_{d,c}\left(\frac{\omega}{c}\right)^2 \tag{4}$$

where ε_d and ε_c are complex permittivities of the dielectric and the conductor, respectively. k_{zd} refers to the dielectric region where $z > 0$ and k_{zc} to the region of the conductor or $z < 0$. Bound plasmons to dielectric/conductor interface have an electric field that decays exponentially in both direction of propagation and polarization.

Non-radiative SPP will occur when the imaginary part of k is larger than its real part and the EM field's penetration depth will be shorter than the wavelength of incident light. Both

radiative and non-radiative SPPs can travel along the interface (x) while their frequency is depends on k_x wavevector which we will call k_{SPP} from now on.

By using Maxwell's equations and considering the continuity of E and H vectors [31], the dispersion of non-radiative SPPs can be calculated. For EM light with p-polarization (meaning that E-field is in plane of propagation while H has just a -y component) one can write:

$$\varepsilon_d k_{zc} + \varepsilon_c k_{zd} = 0 \tag{5}$$

Surface plasmon wave vector or k_x can be re-written as:

$$k_{SPP}(\omega) = \left(\frac{\omega}{c}\right)\sqrt{\frac{\varepsilon_d \varepsilon_c}{\varepsilon_d + \varepsilon_c}} \tag{6}$$

Due to complex nature of ε_d and ε_c, k_{SPP} is also a complex number.

2.2 Drude model

According to the Drude-model [32], the complex permittivity of material can be written as:

$$\varepsilon(\omega) = \varepsilon_\infty \left(1 - \frac{\omega_p^2}{\omega^2 + i\omega\omega_\tau}\right) \tag{7}$$

where ε_∞ is the permittivity of materials well above the bulk plasma frequency (ω_p) and ω_τ is the relaxation frequency which is inverse of relation time or τ. For metals, ε_∞ is generally equals to unity since the charge carrier concentration is sufficiently high. In the IR region, the real part of

permittivity is generally negative and much larger than the imaginary part. Assuming damping is negligible in this region, the permittivity of conductor can be written by

$$\varepsilon_c = \varepsilon_\infty \left(1 - \frac{\omega_p^2}{\omega^2} \right)$$

(8)

Figure 3 show the SPP dispersion relation based on the above equations. In low frequency regime, the dispersion curve follows the light line ($\omega = ck_x$) while for the optical frequencies approaching the limit plasmon dispersion at the interface, wavevector of SPP (k_{SPP}) will approach infinity. For frequencies above plasm frequency, ω_p, the SPPs will be unbound or radiative. As it was mentioned before, in case of noble metals, ε_∞ is unity and for bound surface plasmin modes:

$$\omega \leq \frac{\omega_p}{\sqrt{1+\varepsilon_d}}$$

(9)
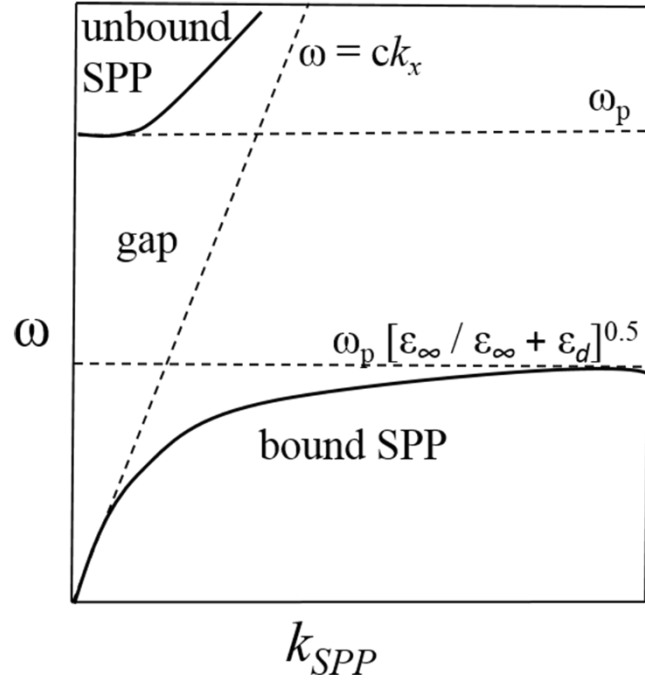
Figure 3 Dispersion relation for bound- and unbound- SPPs.

In the IR region of the spectrum and especially for doped-semiconductors and semimetals, the above assumption of $\omega_\tau \sim 0$ and $\varepsilon_\infty \sim 1$ is no longer valid. As we will see in chapter 3, for some semimetals the can be even up to 100.

The decay length and penetration depth of the SPP electric field is useful in determination of a useful optical coupler for sensing and wave guiding applications. The energy decay length in the propagation direction can be written as:

$$L_x = \frac{1}{2\,\mathrm{Im}(\mathrm{k}_{spp}(\omega))} \tag{10}$$

L_d and L_c are characteristic lengths of 1/e penetration depth of the electric field of SPP into the dielectric and conductor, respectively and are given by:

$$L_{d,c} = \cfrac{1}{\cfrac{\omega}{c} \mathrm{Im}\left(\sqrt{\cfrac{-\varepsilon_{d,c}^2}{\varepsilon_d + \varepsilon_c}}\right)}$$

(11)

2.3 Excitation of SPPs by prism-coupling method

First experimental method of exciting surface plasmon polaritons on flat metal surfaces was introduced by Otto in 1968 [6]. The prism coupling works based on transformation of incident light wave into an evanescent electromagnetic field that may couple to SPP. Figure 4 shows the Otto geometry for excitation of SPPs on flat metal surfaces.
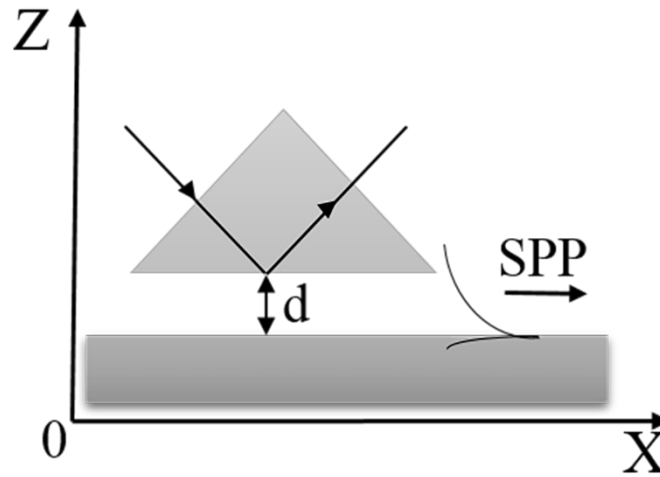
Figure 4 Excitation of SPP via a prism coupler in an Otto configuration.

As it is shown in Figure 4, phase-matching of SPP can be achieved in a three layer system consisting of a metal film sandwiched between two dielectrics with different permittivity values. In Otto's configuration, prism works as a dispersive element with high permittivity value and there is an air gap (or any material with low dielectric value) between metal film and the prism. Plasmonic mode at right angle could be supported at air/metal interface.

11

Total internal reflection (TIR) will occur when refractive index of prism (n_p) is larger than of the outside dielectric (n_d). TIR will take place at the prism base with critical angle $\theta_c = Sin^{-1}(n_p/n_d)$. In the case of TIR excitation, the evanescent field will penetrate through the medium with lower refractive index.

The dispersion for the SPP propagating along the metal/air interface can be written as

$$k_{spp}(\omega) = \frac{\omega}{c}\sqrt{\varepsilon_m(\omega)\varepsilon_d/(\varepsilon_m(\omega)+\varepsilon_d)} \tag{12}$$

while for the evanescent wave from TIR inside the prism, dispersion for the projection of wavevector on the prism base would be:

$$k_{TIR}(\omega) = \frac{\omega}{c}n_p Sin(\theta(\omega)) \tag{13}$$

Figure 5 shows the schematic of dispersion relation involved in prism coupling. Wave dispersion inside the prism is given by $\omega = ck(\omega)/(n_p Sin\theta (\omega))$ while the wavevector projection along the SPP projection is denoted by $k(\omega)$ and is the resonance angle. For an arbitrary angle of incidence, the dispersion falls into between the dispersion curves for incident light inside the dielectric and prism.
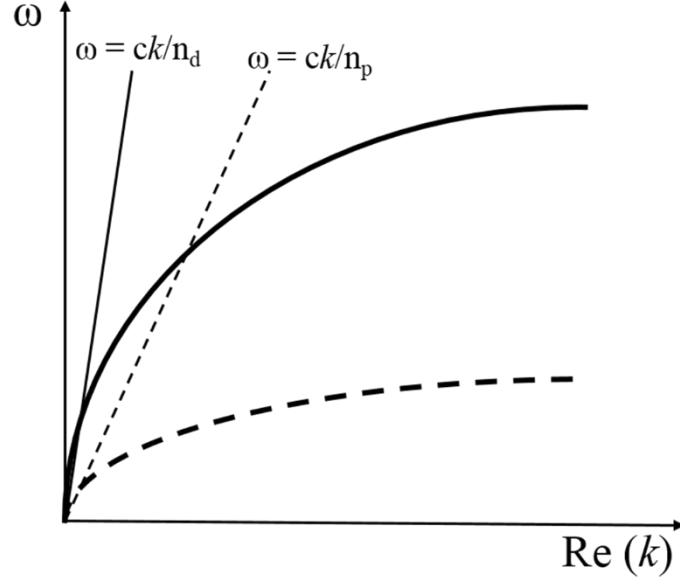
Figure 5 Dispersion relationship in a prism-coupler setup.

At a specific frequency (ω), one can obtain the resonance angle:

$$\theta_{res}(\omega) = \text{arcSin}\left(\frac{1}{n_p} \sqrt{\frac{\varepsilon_m(\omega)\varepsilon_d}{\varepsilon_m(\omega) + \varepsilon_d}} \right) \tag{14}$$

The half width of the resonance angle is given by:

$$\Delta\theta_{res}(\omega) = \frac{c}{\omega} \frac{\text{Im}(\text{k}(\omega))}{n_p \theta_{res}(\omega)} \tag{15}$$

Where $k(\omega)$ is the wavevector of the EM wave and np is the refractive index of the prism.

Two different geometries of SPP prism-coupling are called Otto and Kretschmann configurations and are depicted in Figure 6. In Kretschmann configuration, a thin conductor film is evaporated on top of borosilicate prism. With incident light from the glass side and an angles greater than critical angle, the incident photons will tunnel through the metal film and SPP will be

excited at metal/dielectric interface. As it was discuses earlier, Otto configuration is based on a metal film separated by a thin air gap.
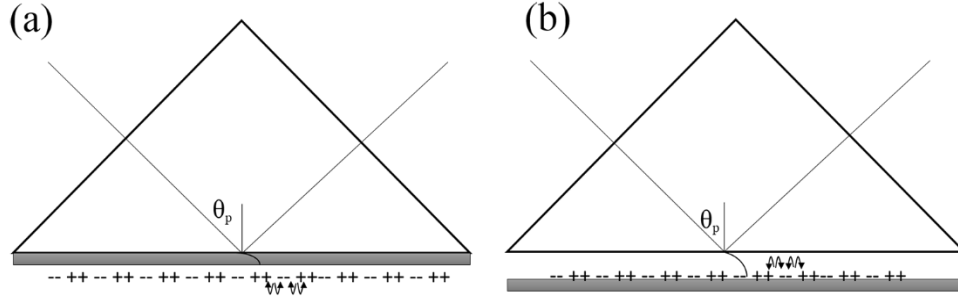
Figure 6 General prism coupling mechanisms for exciting SPPs (a) Kretschmann configuration, (b) Otto configuration.

SPP excitation will manifest itself as a minim in reflectivity spectrum. This minimum is due to destructive interference between the leakage radiation and reflected part of excited beam and its depth depends on thickness of the metallic film. For the optimum thickness, reflectance goes to zero.

2.4 Excitation of SPPs by grating-coupling method

The coupling condition between an electromagnetic wave that is incident from the dielectric at an angle θ on a grating (the plane of incidence is perpendicular to the grating grooves) is:

$$\frac{\omega}{c}\eta_d \sin\theta + m\frac{2\pi}{p} = \text{Re}[k_{spp}] \qquad (16)$$

where m is an integer of either sign which is related to order of diffraction, η_d is the refractive index of the dielectric above the grating and p is the period of grating. Because the

grating can produce the impinging free waves resulted from additional momentum of wavevector arising it periodic structure, the dispersion will have a set of straight lines with of c/Sinθ as it is shown in Figure 7.
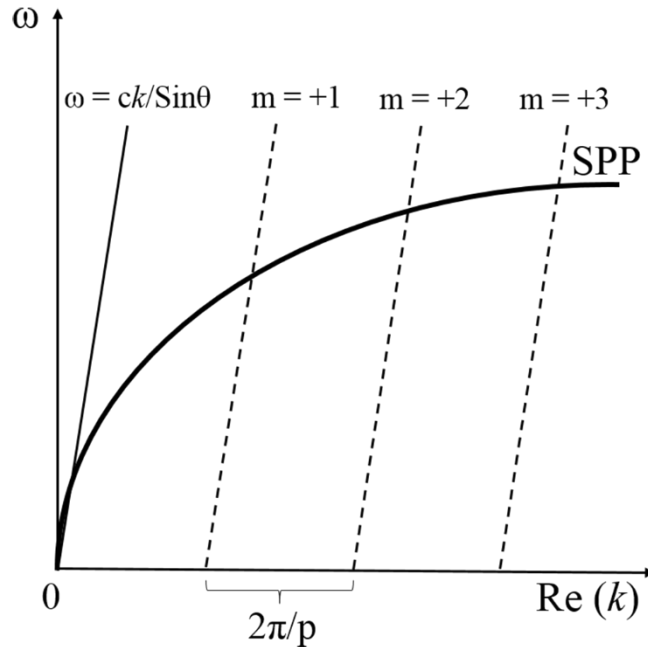
Figure 7 Dispersion in SPR grating coupler.

Figure 7 shows the dispersion curve of a SPP and photon for a fixed angle of incidence, θ. The horizontal axis is the in plane component of the incident EM wave with $k_x = (\omega/c) \sin \theta$, or the real part of the SPP wavevector, while the vertical axis is the photon or SPP frequency. All incident angles are at the same side of surface normal and consequently slopes of all light lines are positive. A resonance occurs for a fixed angle of incidence once a wavevector of an incident wave intersects with SPP dispersion curve. As it is clear for a fixed angle θ, the resonance could happen for both positive and negative k_x values.

Grating couplers with high efficiency have been reported before [33]. In fabrication of gratings one should be very careful to get the right period and height to get the sharpest possible surface plasmon resonances. Also, due to nature of momentum matching of gratings, only one frequency can be efficiently coupled to a SPP which makes them unsuitable for broadband measurements.

2.5 Optical characterization of SPP hosts by ellipsometry

Complex permittivities of optically thick thin-films were carried out in a J.A. Woollam IR-VASE and V-VASE ellipsometers in the infrared and visible wavelengths, respectively. The two raw ellipsometer outputs are the complex reflectance of a p-polarized light to s-polarized, Ψ and the phase shift, Δ between the two complex reflectances. The complex permittivity data ε, can then be calculated from values of Ψ and Δ at each wavelength.

The optical skin depth of SPP hosts can be determined from two different methods. By having the value of complex permittivity, ε the optical skin depth, δ is given by:

$$\delta = \frac{1}{k \, \omega/c} \tag{17}$$

where k is the extinction coefficient and is directly obtained from ellipsometry measurements.

In addition, by having the transmittance of two thin-films and knowing their respective thicknesses, the optical skin depth can be accurately determined according to:

$$\delta = \frac{2(d_2 - d_1)}{\ln\left(T_1(\lambda)/T_2(\lambda)\right)} \tag{18}$$

where d and T are thickness and transmittance of each film, respectively.

CHAPTER THREE: SURFACE POLARITONS ON BISMUTH

3.1 Introduction

Here we will investigate the infrared surface plasmon polaritons on the semimetal bismuth (Bi). The complex permittivity has been measured before from visible to far-infrared wavelengths, but the samples studied have been oriented single crystals or melt-cast and mirror-polished polycrystalline samples. Evaporated Bi films are more likely to be used in applications, and an unanswered question is how the optical properties of these films compare with those for crystalline samples. To this end, we measured the permittivity spectra for electron-beam and thermally evaporated Bi films by ellipsometry from 1.4 to 40 μm wavelength. To validate the measured optical constants, we measured far-infrared reflectivity spectra on smooth Bi films and long-wave-infrared optical excitation resonances for SPPs on Bi lamellar gratings. These measurements were shown to agree well with calculations based on our permittivity values.

A motivation for this study was that SPP modes on Bi have potential nanophotonic device applications due to their tight IR confinement when compared to traditional plasmon hosts such as noble metals. Tightly bound SPPs in the IR molecular fingerprint range could be used for real-time sensing of biomolecule interactions on suitably functionalized surfaces [17, 34].

3.2 Theoretical model of permittivity of bismuth

The long-wavelength permittivity of a conductor can usually be described by a modified-Drude model:

$$\varepsilon = \varepsilon_\infty \left[1 - \frac{\left(\dfrac{\omega_p}{\omega} \right)^2}{1 + i \left(\dfrac{m}{m^*} \right) \left(\dfrac{1}{\omega\tau} \right)} \right] \qquad (19)$$

where τ is the relaxation time, $\boldsymbol{\varepsilon}_\infty$ is the real part of permittivity well above the plasma frequency, which we defined here,

$$\omega_p^2 \equiv \frac{4\pi N e^2}{m^* \varepsilon_\infty} \qquad (20)$$

This definition (in Gaussian units) is somewhat different than in [35]. This is done so that in the case $\omega\tau \gg 1$ when ε is real, the value of ω_p would be the frequency at which the permittivity changes sign. Then ω_p has the same physically-intuitive interpretation as for good metals, for which $\varepsilon_\infty = 1$ and $m = m^*$. In the case of bismuth near the zero crossing of ε', we actually have $\omega\tau \sim 1$, so that the zero crossing frequency is red shifted and has the value $\sqrt{\omega_p^2 - \left(\dfrac{m}{m^*} \right)^2 \tau^{-2}}$.

Using values of $m^*/m = 0.92$ and $\tau^{-1} = 270$ cm^{-1} from [35] allows us to determine ω_p from the zero crossing of ε', and we are left with the single parameter ε_∞ to fit Eq. (19) to the $\boldsymbol{\varepsilon}_\infty$ spectrum. For completeness, we give the formulas for ε' and ε'':

$$\varepsilon' = \varepsilon_\infty \left(1 - \frac{\left(\dfrac{\omega_p}{\omega} \right)^2}{1 + \left(\dfrac{m}{m^*} \right)^2 \left(\dfrac{1}{\omega\tau} \right)^2} \right) \qquad (21)$$

$$\varepsilon'' = \frac{\varepsilon_\infty \left(\dfrac{m}{m^*}\right)(\omega_p \tau)^2}{\left((\omega\tau)^2 + \left(\dfrac{m}{m^*}\right)^2\right)\omega\tau}$$ (22)

When $\omega\tau \ll 1$, the limiting form of ε'' goes as $1/\omega$, as it should [31]. Far infrared reflectivity spectra are calculated from the complex permittivity spectra according to Fresnel's equations, namely

$$R = \left|\frac{1-\sqrt{\varepsilon}}{1+\sqrt{\varepsilon}}\right|^2$$ (23)

This same expression was used to obtain an ε' spectrum from experimental values of ε'' and R presented in [35].

3.3 Experimental details

Bismuth films were thermally and electron-beam evaporated from 99.999% pure Bi pellets onto one-sided polished (100) silicon substrates. Multiple evaporations were required to build-up an optically thick layer, with each layer thickness confirmed using a Veeco Dektak step profiler. The infrared penetration depth into Bi was estimated from infrared transmittance spectra for films of different thicknesses to be ~ 3 μm at 10 μm wavelength [36, 37]. A thermally-evaporated Bi film of 12 μm thickness was prepared for ellipsometry measurements, and this sample was considered optically thick, such that no transmitted light reached the substrate.

An electron-beam evaporated film of 6 μm thickness was also studied, but even though this was twice the characteristic penetration depth, there was evidence in the ellipsometry and reflectivity spectra of Fabry-Perot fringes, indicating penetration to and reflection from the

substrate. A study of the thickness dependence of the amplitude of these fringes was published in [36] and showed that the fringe amplitude decreases monotonically and are no longer observable for thicknesses of 8 microns and higher.

The Bi films were characterized by a J.A. Woollam IR-VASE ellipsometer, which spans the wavelength range 1.4 to 40 μm. The complex permittivity spectrum was calculated from the raw ellipsometer output using standard Fresnel equations [31, 38], assuming no contribution from the substrate.

The normal-incidence far-infrared reflectivity spectrum was measured using a Bomem DA8 spectrometer with reflectivity accessory inside the evacuated sample compartment. The resources used were a globar source, mylar pellical beamsplitters of thickness 3 and 6 μm, and a room temperature DTGS detector. The useful spectral range for these measurements was 50 to 700 cm^{-1} (200 to 14 μm wavelength).

Lamellar gratings for SPP generation experiments were fabricated by photolithography. A ~1 μm thick layer of photoresist was spun on Si substrate followed by UV exposure under a grating mask with 20 μm period and 50% duty cycle. This was followed by development in Tetramethylammonium hydroxide (TMAH) based solution. A thick Bi coating was thermally evaporated on the gratings. The grating profile was characterized by cross-sectional scanning electron microscopy (Hitachi FE-SEM SU-70).

The reflectance of the grating was measured using a tunable quantum cascade laser (QCL) from Daylight solutions with specular resolution of 0.1 nm. The incident radiation was tunable in the range of 7.9 μm to 10.5 μm, and was digitally chopped at 1 kHz. A mercury cadmium telluride (MCT) detector was used to measure the reflected intensity, utilizing a lock in amplifier to

demodulate the signal at the chopping frequency. With the QCL fixed, the sample and detector were rotated to perform angular reflectance measurements as it is shown in Figure 8.
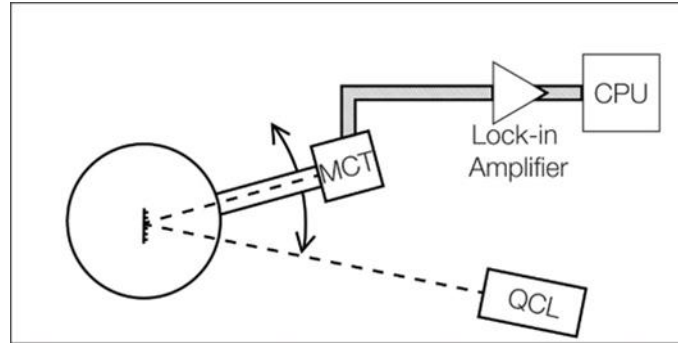
Figure 8 A schematic showing the experimental setup. A fixed QCL was used to excite surface plasmon modes in a bismuth grating fixed to a motor controlled goniometer. The MCT detector was positioned at twice the incidence angle, and a lock in amplifier was used to record the intensity.

.

The completed grating was mounted on top of a motor controlled goniometer for precise control over the incidence angle of the incoming radiation. The detector was mounted on an arm of the goniometer and programed to move twice the angular distance of the sample, in order to track the primary reflection. The grating rulings were positioned to be orthogonal to the TM-polarized beam. A custom LabView program was used to record the signal from the lock in, in addition to controlling the angle of incidence and the wavelength of the source. A background measurement was performed after each measurement by replacing the grating with a gold mirror. The reflectance was then found by dividing the grating spectrum by the background signal.

Angular reflectance measurements were performed at a fixed excitation wavelength, as the sample and detector are rotated. Stepper motors capable of one hundredth of a degree accuracy were used to rotate the sample from 5 to 80 degrees angle of incidence. A fixed angle of incidence was used to perform the specular reflectance measurements. The wavelength of the source was

incremented by 5nm over the full range from 7.9 to 10.5 μm. The specular reflectance of the bismuth grating is shown later in results section.

3.4 Characterization of bismuth thin-films

Figure 9 present SEM images of the surfaces of thermally and electron-beam evaporated Bi films. The thermally evaporated sample is composed of nano-crystals of Bi with characteristic lengths of 100 to 200 nm. The electron-beam evaporated film has larger average particle in the range 200 to 600 nm. Differences in the porosity and concentration of boundaries for the two films are expected to cause their permittivity spectra to differ from each other and from that of single crystal Bi.

(a)

200 nm
Mag = 100.55 K X   EHT = 5.00 kV
Signal A = InLens   WD = 4.5 mm

(b)

200 nm
Mag = 100.55 K X   EHT = 5.00 kV
Signal A = InLens   WD = 4.5 mm
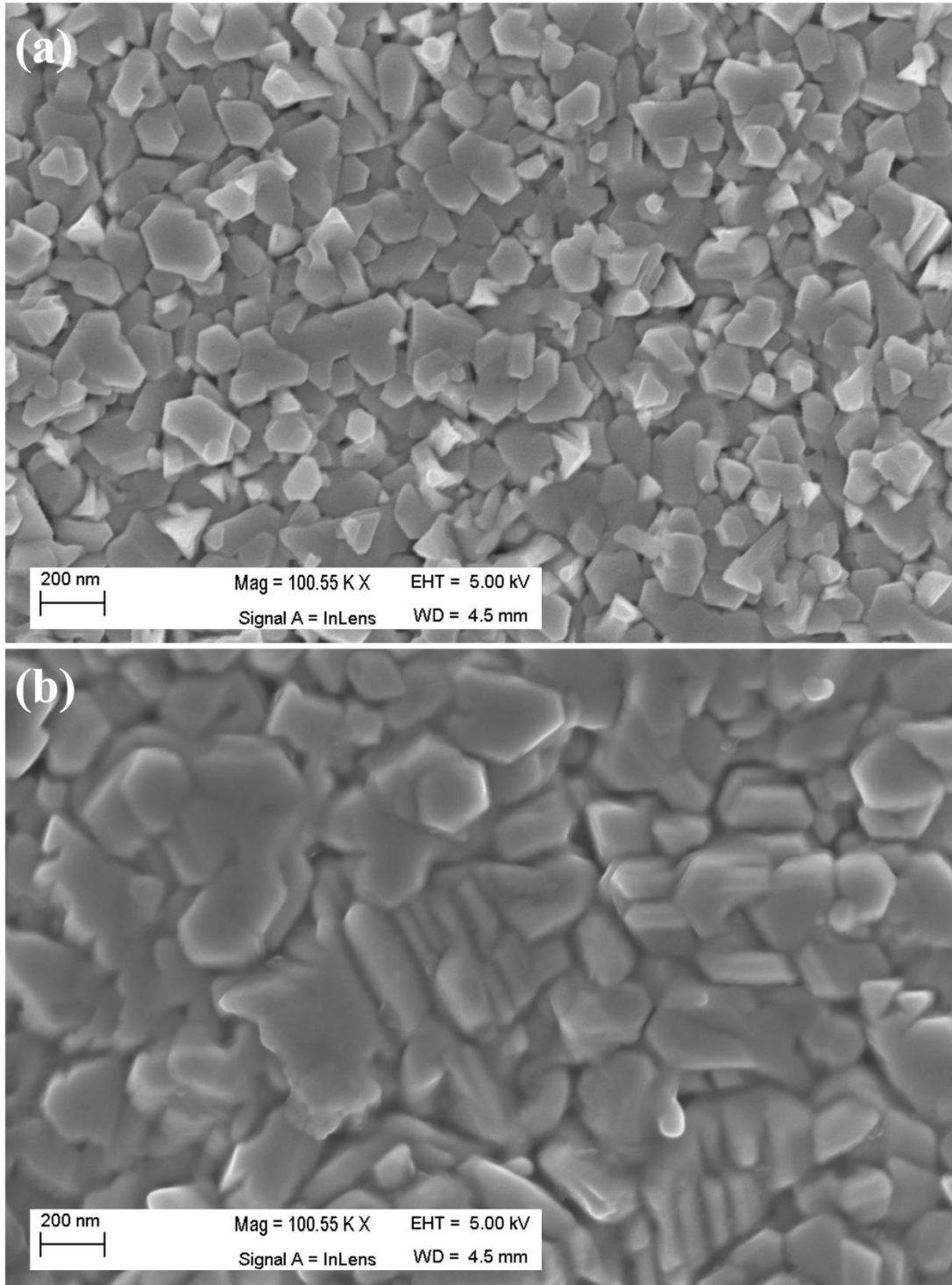
Fig. 9. SEM image of (a) thermally evaporated (b) e-beam evaporated Bi thin films.

Figure 10 presents XRD θ-2θ measurement of both thermal and e-beam evaporated Bi films. The e-beam evaporated Bi films exhibit only reflections from (003), (006) and (009) planes, which suggests that the Bi trigonal axis is oriented perpendicular to the substrate. The thermally evaporated film has additional reflections from (104), (202), suggesting a lower degree of orientation. The broad weak peak at 69 deg is due to the substrate, as confirmed by its disappearance when the sample is tilted slightly off-normal to the plane of incidence. All of the sharp peaks belong to crystalline Bi. If the interpretation of the SEM images as being overlapping nano-crystalline platelets is correct, the larger platelets for the e-beam evaporated sample might give a more oriented, less jumbled, pile of particles, which would explain the difference in the XRD results.
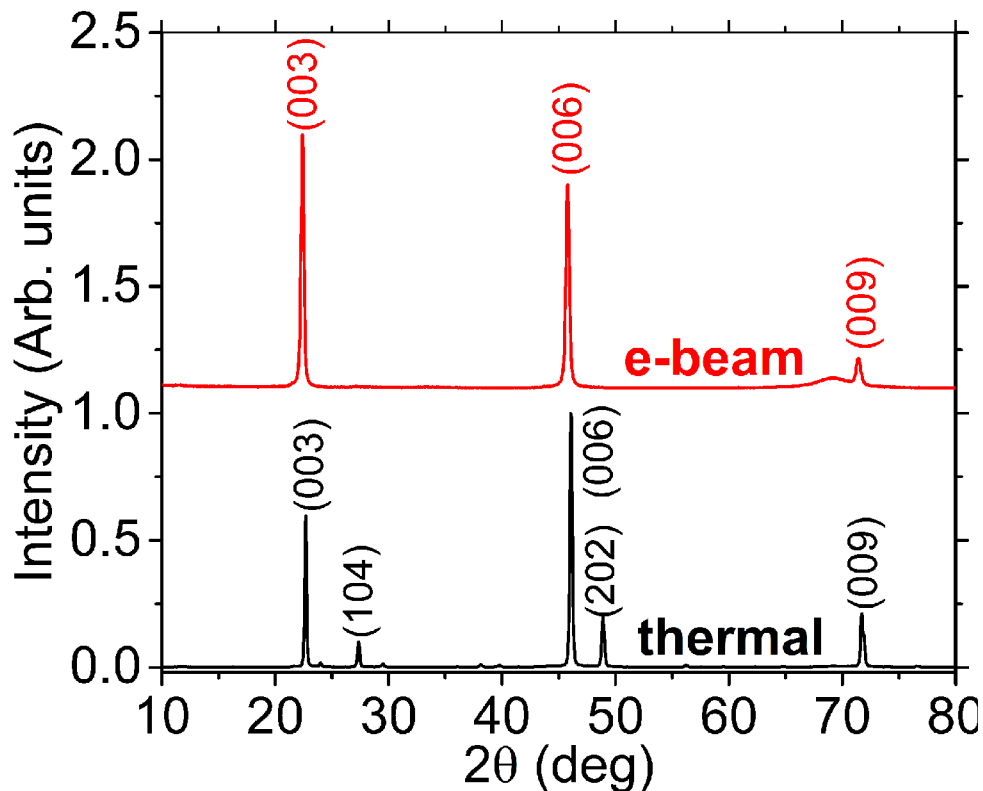
Figure 10 XRD of thermally and e-beam evaporated bismuth films.

The complex permittivity spectra of our Bi films are presented in Figure 11. The ε' values are negative beyond ~31 μm wavelength, which indicates a smaller plasma frequency than for Sb, where the cross-over occurs at 11 μm [27]. The ε'' values are positive over the whole spectrum, as thermodynamically required [31]. In the wavelength region of our SPP studies (8 to 10.5 μm), $\varepsilon' > 0$ and its value is comparable to that of ε''. This situation is similar to that of Sb in the same region, where bound SPP waves were demonstrated [27].
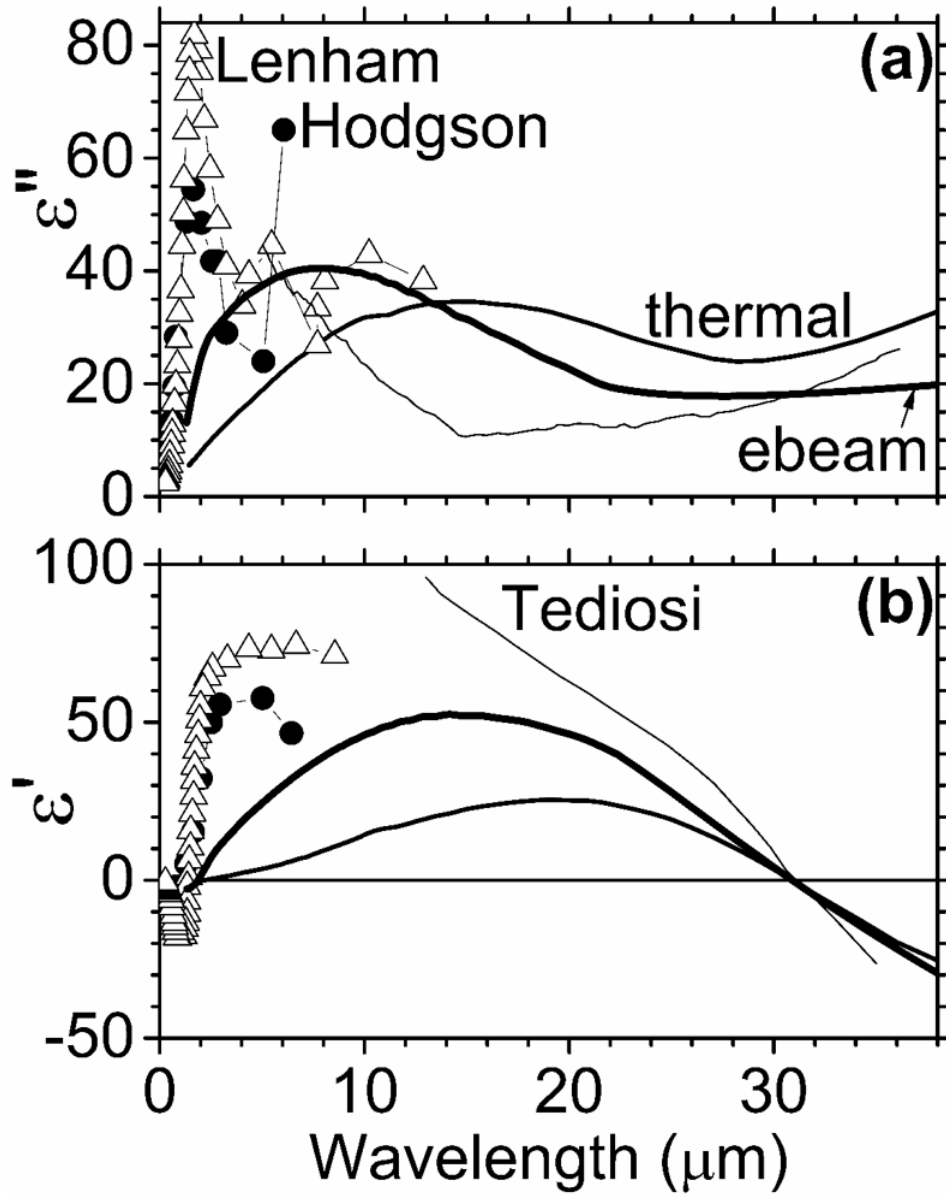
Figure 11 Permittivity spectra for thermally and electron-beam evaporated bismuth. (a) Imaginary part. (b) Real part. Comparison is made to prior reports for melt-cast polycrystalline or trigonally-oriented crystalline samples.

Comparison is made in Figure 11 with previous near- to long-wave IR results for melt-cast polycrystalline Bi [39] and for oriented single crystal [35, 40] Bi. The short-wave permittivity values for the evaporated films are significantly smaller. This may be a consequence of porosity

and grain boundaries in the evaporated film. The e-beam evaporated film has higher permittivity values to shorter wavelength than does the thermally-evaporated film, and this may be explained as due to its larger grains so that the film behaves more like continuous metal.

The permittivity spectrum of Tediosi et al. [35] for single crystal Bi oriented along the trigonal axis is the only other published result for wavelengths longer than 12 microns. Their ε' data are determined from their presented normal incidence reflectivity spectrum R and the ε'' values that we calculated from their presented conductivity spectrum, $\varepsilon'' = \sigma/\varepsilon_0\omega$ in S.I. units, where ε_0 is the vacuum permittivity [35].

The reflection from an optically thick bismuth thin film at normal incidence can be written according to Eq. (23). By plugging in the measured values for ε'' from Tediosi et al. [35] and R from normal reflection measurements, ε'' can be calculated at each wavelength. Figure 12 represents two possible solutions for ε' but considering the fact that the real part of permittivity is negative below plasm frequency and first derivative of ε' relative to frequency is always positive, $d\varepsilon'/d\omega > 0$, only one solution is physical. Calculated ε' is positive below plasm frequency and crosses zero at 31 microns. Above the zero crossing wavelength, the value of real permittivity is negative and its magnitude increases by increasing wavelength.
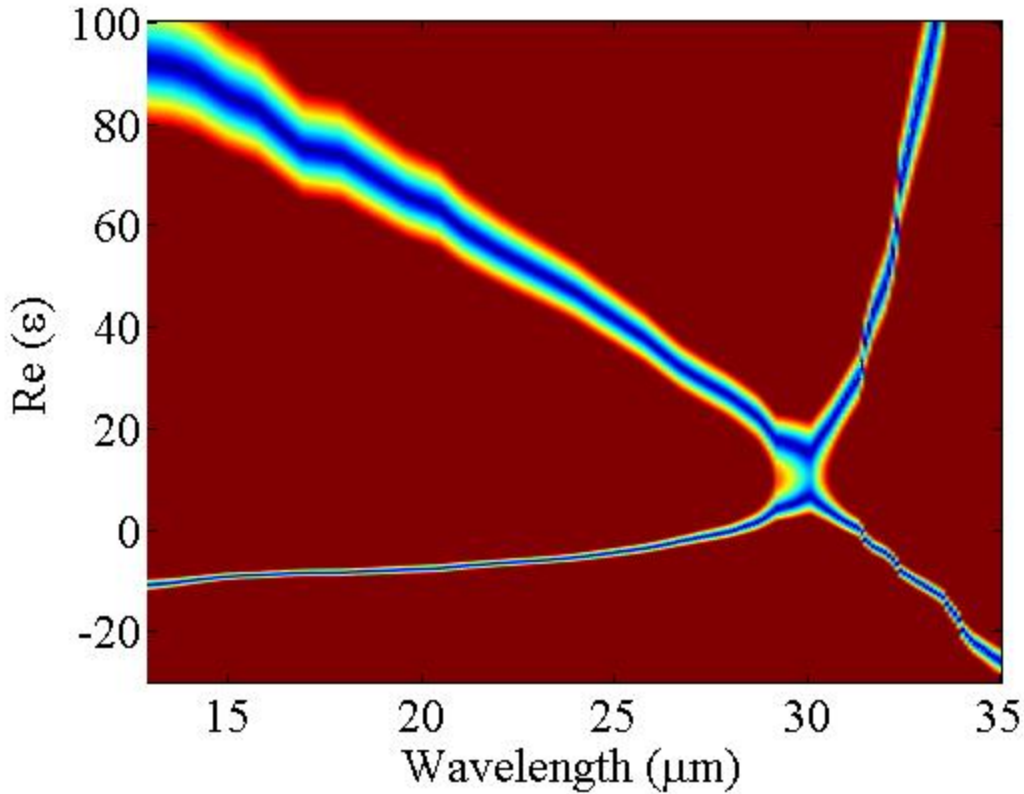
Figure 12 Calculation of real permittivity of bismuth from values of reflectivity and imaginary part of permittivity.

Significant differences in the ε'' values for the three curves point to loss mechanics of morphological rather than fundamental origin. The larger grained electron-beam evaporated sample may be expected to behave more like a continuous film, and its ε'' spectrum is indeed closer to that of the single crystal result as it is shown in Figure 11

Using the observed zero crossing at 30.86 μm for ε', together with values for τ and m^* from [35], determines the value $\omega_p = 437$ cm^{-1}. Then, fitting Eq. 21 to the Figure 11 spectrum in the range 30-38 μm determines the ε_∞ value to be 112, which is essentially the same as the value 108 given in [35]. The spectrum for the thermally-evaporated film and the fit are presented in

Figure 12, and the agreement is excellent for wavelengths of 30 μm and beyond. (The spectrum

for the e-beam evaporated film is very similar). From Eq. 20, we determine the concentration of

carriers to be 2.2 x 10^{20} cm^{-3}, which is at least 20x larger than the values previously reported for

molecular beam epitaxy (MBE) grown films [41].
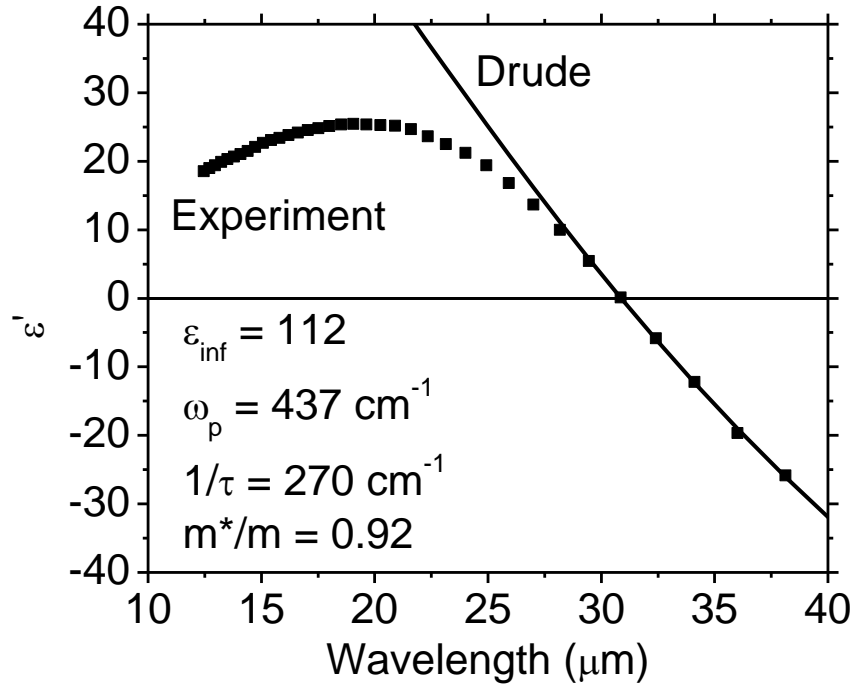
Figure 13 Permittivity spectrum compared to Drude calculation. The real part of the permittivity for the thermally evaporated film is plotted as symbols, while the Drude calculation is given by the solid line. Drude parameters used are indicated.

Calculated ε'' spectra from Eq. (22) gives poor agreement with experimental results in both

shape and magnitude. This indicates that the main source of far-infrared loss is something other

than free electron absorption at these wavelengths. A possible source is multi-phonon absorption,

but the difference between thermal and e-beam evaporated samples shows that there are also losses

of technological, rather than fundamental, nature.

Figure 14 compares measured reflectance for an e-beam-evaporated 6-µm-thick bismuth film with calculations Eq. (23) and with prior measurement [35]. The measured spectrum shows Fabry-Perot oscillations because the film thickness is only twice the skin depth and there is a large index mismatch between the Bi (ε' ~ 40-50, see Figure 11) and the silicon substrate ($\varepsilon' = 11.7$) at these wavelengths. The similarity between calculated and measured R spectra confirms our ellipsometer-measured permittivity spectra. The minimum of reflectance occurs at ~ 343 cm^{-1}, and the absorption feature is somewhat broader and deeper than reported earlier for the crystal sample [35].
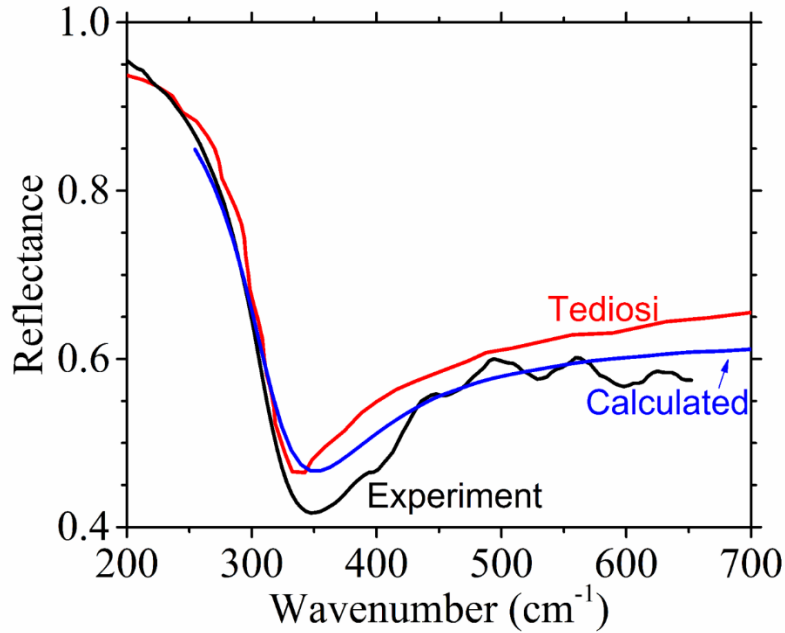
Figure 14 Measured and calculated reflectance from an e-beam made Bi sample is compared with Tediosi et al..

The SPP propagation length L_x and field penetration depths $L_{d,c}$, calculated from permittivity data using Eqs. (11 and 12), are presented in Figure 15. A broad shallow dip for Bi

occurs around 31 microns where ε' changes sign. At 10 μm wavelength, L_x is around 400 μm. Here, $L_d \sim 100$ μm and $L_c \sim 3$ μm.
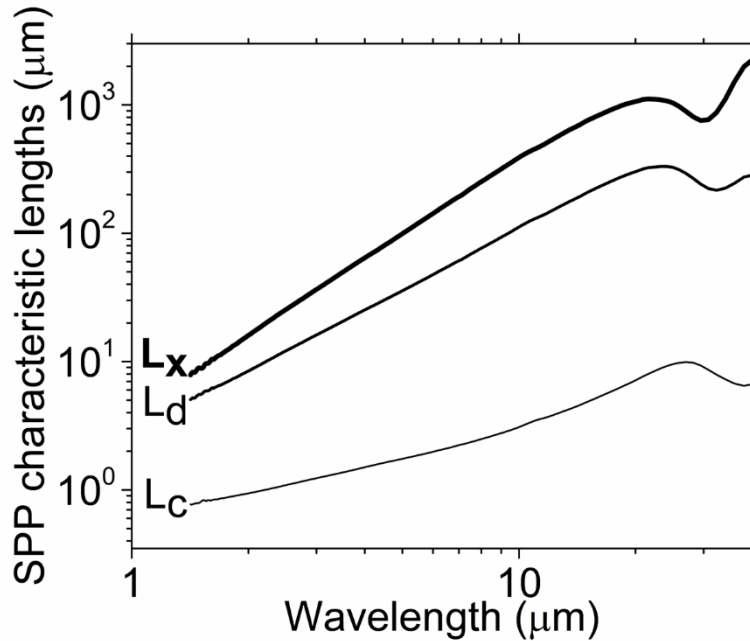
Figure 15 Surface plasmon polariton characteristic lengths as a function of free-space wavelength (top) Propagation length L_x. (bottom) Penetration depth in dielectric (L_d) and conductor (L_c), respectively.

Figure 16 presents an SEM image of the grating profile. The average groove depth is 2.0 μm. The thickness of the thermally-evaporated Bi is 1.4 μm, which is only half the penetration depth at 10 microns wavelength, so that the SPP fields will penetrate to the Si and photoresist. Due to the coating of the groove side walls, the duty of the grating bars is ~ 65%, i.e. it exceeds the 50% duty cycle of the photomask.
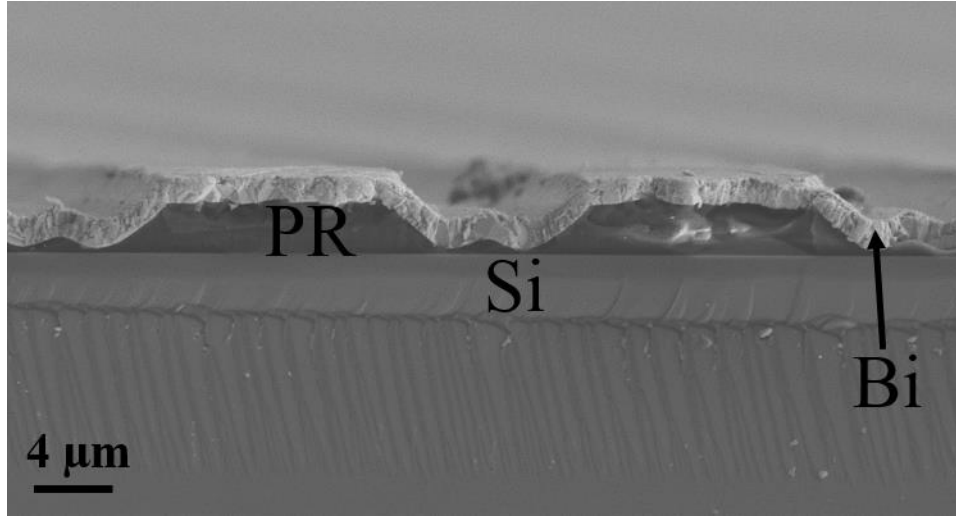
Figure 16 SEM cross section of bismuth gratings. Si substrate, photoresist ridges (PR), and thermally-evaporated Bi coating are indicated.

Figure 17 (a) presents measured and calculated reflectance spectrum from the Bi grating at 64 deg angle of incidence. The values plotted are normalized reflected intensity with the QCL wavelength stepped in 5 nm intervals from 8 to 10.5 μm wavelength. A resonance due to excitation of SPPs appears near 9.5 microns, which agrees with Eq. (16) for the m = -4 order. The calculated spectrum (scattering matrix method [8, 9]) that gave the best agreement (plotted) assumed a grating amplitude of 1.4 μm and a grating-bar duty of 65%, values somewhat smaller and larger, respectively, than obtained for the actual grating. Calculations using our permittivity values and those of [40] for crystal Bi are very similar despite a ~5-fold difference in ε' values, although the width of the resonance calculated using the published spectrum is closer to what is observed.

A resonance due to excitation of SPPs appears near 9.4 μm wavelength, in agreement with Eq. (16) for the m = 1 order. Figure 17 (b) presents the measured and calculated reflectance spectrum from Bi gratings at 32 deg of incidence. The calculated spectrum with best agreement

32

assumes a grating with amplitude of 1.8 μm and duty cycle of 70%. Again, the calculation based

on the published permittivity gives a resonance width in closer agreement with observation.
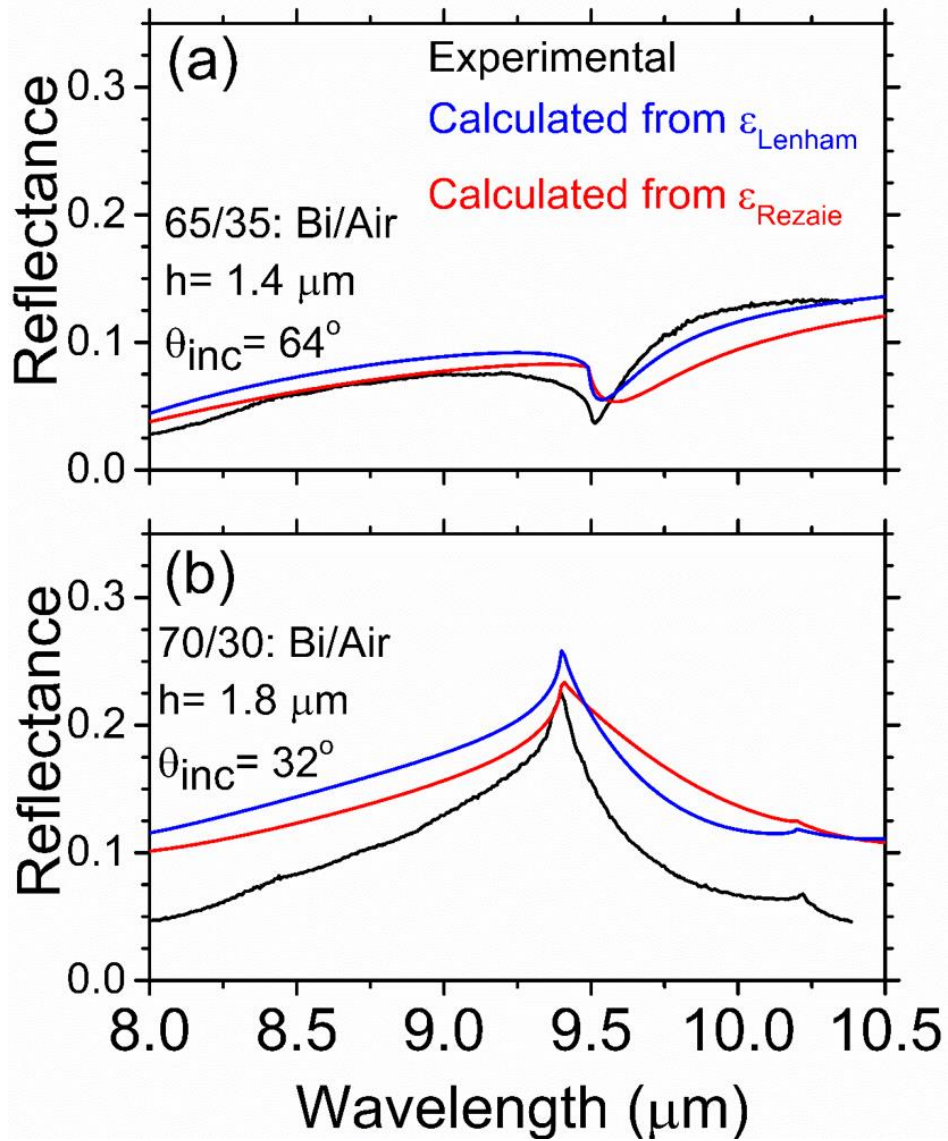
Figure 17 Specular reflectance of Bi gratings at (a) 64 degrees angle of incidence, m = -4 resonance order. (b) 32 degrees angle of incidence, m = 1 resonance order.

Figure 18 presents experimental reflectance spectra for the m = -4 resonance at different

angles of incidence. Resonances sharpen and red-shift as the incidence becomes more oblique.

This order's absorption is sharper and more resonance-like, and hence more interesting for sensing applications.
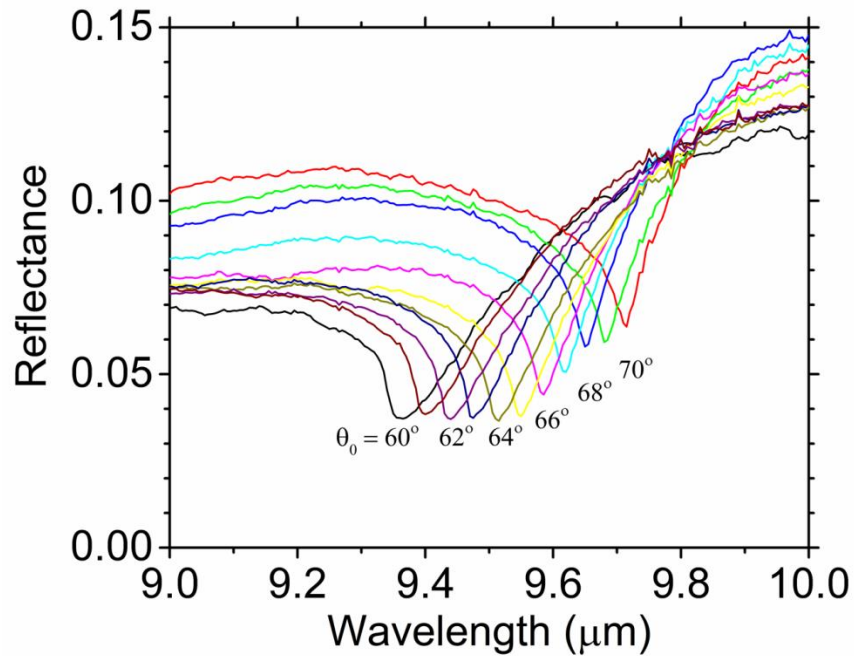
Figure 18 Reflectance spectra for Bi gratings at different incidence angles corresponding to the m = -4 resonance.

In summary, we have measured permittivity spectra for evaporated bismuth films in the range of 1.4 to 40 microns. These spectra differ significantly from those previously published for oriented single crystal or melt-cast polycrystalline Bi, and the spectra for thermal and e-beam evaporated films differ from each other. We studied the excitation resonances for infrared SPPs in evaporated Bi gratings, and we found that calculated spectra based on our permittivity values agree well with the observed spectra. The IR resonances in the range of 8-10.5 microns are distinct and potentially useful in sensing applications. Hence Bismuth, whose plasma frequency is more

than two orders smaller than traditional metal hosts such as Au, has potential for mid- to long-wave IR plasmonic applications.

CHAPTER FOUR: FLOURINE DOPED TIN OXIDE THIN FILMS BY STREAMING PROCESS FOR ELECTRODELSSS ELECTROCHEMICAL DEPOSITION (SPEED)

4.1 Introduction

Transparent conducting oxides (TCOs) are wide band-gap semiconductors with relatively high free-electron concentration, which arises either from defects or extrinsic dopants with shallow levels near the conduction band edge [42, 43]. TCOs are increasingly used in photovoltaic (PV) devices and as electrodes, structural templates, and diffusion barriers. TCO work function defines the device open-circuit voltage [44]. Examples of TCOs include ZnO, In_2O_3/SnO_2 (ITO) and SnO_2: F (FTO).

Among TCOs, indium tin oxide is the most widely used [45, 46] because of its high electrical conductivity and optical transparency. Use of ITO has the disadvantage of the scarcity and expense of indium (In), whose price rose due to market demand to over \$800 per kg in 2006. This motivates the search for alternative TCOs. Fluorine-doped tin oxide (FTO) is a promising candidate due to its chemical stability, electrical conductivity, optical transparency, and thermal stability, especially in high-temperature hydrogen-containing environments for gas sensing applications [47-49]. These properties, however, depend on the deposition technique and growth conditions.

The microstructural, electrical, and optical properties of FTO are sensitive to deposition technique and conditions [50]. Methods for SnO_2 thin-film deposition have included ultrasonic chemical spray [51], spray pyrolysis [52], reactive sputtering [53], sol-gel spin coating [54], magnetron sputtering [55-57], and photochemical vapor deposition [58]. Reactive sputtering and evaporation are high vacuum techniques, which makes them expensive for large-scale production.

The films produced by chemical vapor deposition require large volumes of expensive high purity precursors for large area coatings. Films prepared by most spray pyrolysis methods are non-uniform and full of voids and other defects due to uncontrolled droplet sizes and the precursor chemistry [59].

4.2 Streaming Process for Electrodeless Electrochemical Deposition (SPEED)

Streaming Process for Electrodeless Electrochemical Deposition (SPEED) [60-62] is a high-rate uniform deposition technique that uses water-soluble precursors to rapidly coat the substrate with nanoparticle-based films. There are no fundamental limits to the achievable film thickness. SPEED allows high-quality film growth on large area hydrophilic rigid or flexible substrates, at lower temperature than the traditional spray pyrolysis, using environmentally friendly water-soluble primary chemicals and very flexible chemistry formulation for binary or more complex compound materials growth. SPEED allows high-quality film growth on large area hydrophilic rigid or flexible substrates, at lower temperature than the traditional spray pyrolysis, using environmentally friendly water-soluble primary chemicals and very flexible chemistry formulation for binary or more complex compound materials growth. Here we report application of SPEED to grow SnO_2: F thin films.

SPEED has is foundation in chemical bath deposition (CBD) [60, 62, 63] and is distinct from spray pyrolysis. To be pyrolysis, there must be a thermochemical decomposition of organic material at elevated temperatures (> 400 °C) in the absence of oxygen. Indeed, the Greek root "lysis" means "separating". Organic solvents are used, and the products of the decomposition then react to form a film. In contrast, SPEED is a pure heterogeneous reaction between two reactants at a surface, using water as the primary solvent. Without the need to thermally decompose

anything, SPEED is capable of growing materials at much lower substrate temperatures than is spray pyrolysis.

There are no fundamental limits to the achievable film thickness. SPEED allows high-quality film growth on large area hydrophilic rigid or flexible substrates, at lower temperature than the traditional spray pyrolysis, using environmentally friendly water-soluble primary chemicals and very flexible chemistry formulation for binary or more complex compound materials growth. Here we report application of SPEED to grow FTO films.

4.3 SPEED for fluorine-doped tin oxide deposition

The main precursors in the reagent solution are 0.4 M tin IV chloride (the Sn source) and ammonium fluoride (the F source, at 20% of the Sn concentration). The chemicals (Alfa Aesar) were dissolved in a mixed solvent of water, ethanol, isopropanol, and methyl propanol. Deionized water (20% by volume) is one of the main requirements in SPEED chemistry [60], serving as both solvent and oxygen source. The ethanol, isopropanol, and methyl propanol are mainly complexing agents for Sn ions. The complexing capabilities of the mixed solvents controls solution stability and shelf life.

A reservoir of the solution is maintained at a temperature sufficiently low to inhibit homogeneous reactions. The solution was nebulized into droplets (5 - 15 μm size range) by an ICP/MS nozzle and sprayed onto the heated substrate. Before deposition, the 5.0 cm × 5.0 cm substrates were cleaned thoroughly with industrial soap, rinsed with deionized water followed by acetone, then rinsed again with deionized water, and hot-air dried. The film deposition was done by scanning the surface of the vacuum-chucked substrate with the sprayer in cycles. A

proportional-integral-derivative (PID) controlled heater maintained the substrate temperature at 440, 460, 470, or 500 °C. Fig 1 presents a photograph of the SPEED system during deposition.
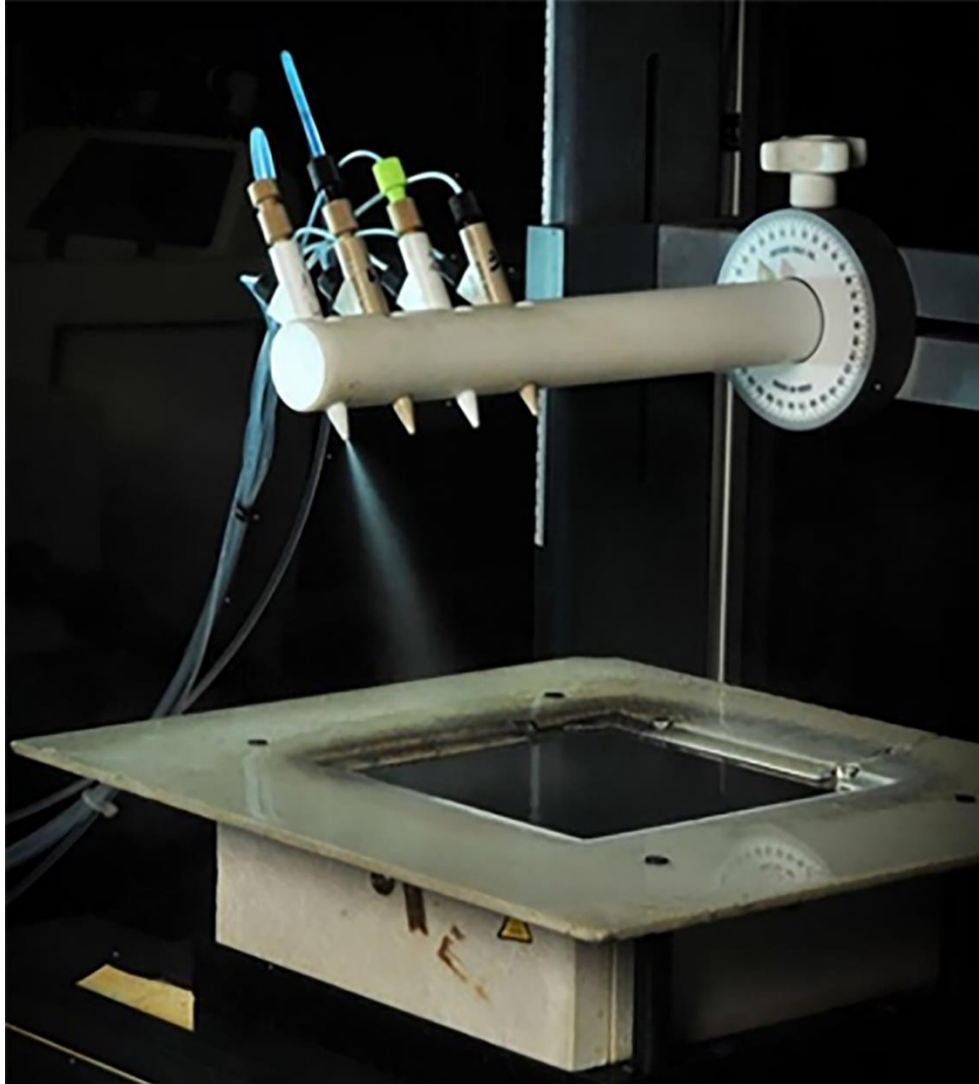
Figure 19 Photograph of SPEED spray head.

SPEED processes and chemistries, have their foundation in chemical bath deposition (CBD) [60, 61, 63] and they are designed to ensure film growth takes place via heterogeneous

reaction only. A process requirement is a hydrophilic substrate that attaches OH⁻ ions, which serve as heterogeneous-reaction nucleation sites. The local electrical field created by the adsorbed OH⁻ to the substrate attracts the positively charged complex to initiate the electrochemical reaction process without an external electrical field, which eliminates the need for electrodes. Similar to what we have in CBD [63], the reactions that summarize the film growth are:

$$[Sub](OH)^- + [SnL_n]^{p+(4+)} \rightarrow [Sub]Sn(OH)^{3+} + (L_n)^p \uparrow \quad , \tag{24}$$

$$[Sub]Sn(OH)^{3+} + 3OH^- \rightarrow [Sub]SnO_2 + 2H_2O\uparrow \quad , \tag{25}$$
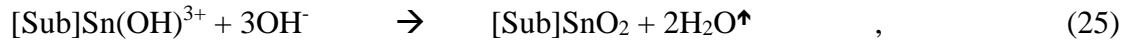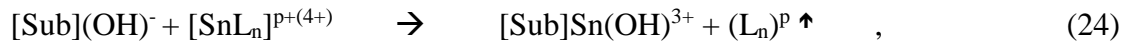
where L is the ligand supplied by the organic solvents, [Sub] is the heated substrate, p is the charge of the ligand L, and n is the number of ligands involved in the Sn/L coordination. The upward arrows signify reaction byproducts that are decomposed and volatilized. The substrate kT must exceed the heterogeneous reaction activation energy and sufficient to decompose and volatilize the reaction byproducts. Formation of attached SnO_2 in Eq. (25) is followed by site regeneration according to

$$[Sub]SnO_2 + OH^- \rightarrow [Sub]SnO_2(OH)^- \tag{26}$$

The attachment of fresh OH$^-$ from a freshly sprayed precursor initiates the next growth cycle, which continues thus layer-by-layer. The high concentration of OH$^-$ nucleation sites causes lateral grain growth competition, leading to nanoparticle morphology of the resulting film. The fluorine doping reaction is

$$[Sub]Sn(OH)^{3+} + 4NH_4F + 3OH^- \quad \rightarrow \quad [Sub]SnF_4 + 4H_2O\uparrow + 4NH_3\uparrow . \qquad (27)$$

Growth of SnF$_4$ molecules occur randomly during growth. F on the O lattice site is a donor. Oxygen vacancies occur via adsorption of the tin complex $[SnL_n]^{p+(4+)}$ according to

$$[Sub][SnL_n]^{p+(4+)} + mOH^- \quad \rightarrow \quad [Sub]Sn + m(OHL_n)\uparrow \qquad (28)$$

With solvent ligands, the adsorbed complex undergoes hydroxyl-ion-assisted reduction to form attached Sn [59], which paired with the oxygen vacancy acts as an donor [52].

4.4 Characterization of Fluorine-doped tin oxide thin films grown on glass substrate

With our current precursors we have observed that transparent and conductive films are grown only when the substrate is subjected to at least 400 ^{o}C. This is the temperature at which the heterogeneous reaction for the formation of SnO$_2$ is overcome, and the reaction byproducts are decomposed and volatilized. However, most of our depositions were carried out at 440 ^{o}C to 500 ^{o}C. At these temperatures, adhesion of the grown film to the substrate is very strong. The film is

plastic-object scratch resistant due to the heterogeneous film growth mechanisms and high crystallinity, since higher cohesive strength is associated with smaller free volume [64, 65].

Initial films were grown on borofloat and quartz glass substrates. As-grown films on quartz have lower resistance than films grown on borofloat glass. Annealing both in vacuum at 450 ^{o}C causes their resistances to increase, with the film on borofloat glass still giving the highest value. Poor results when using borofloat glass substrates may be attributed partially to diffusion of boron impurities into the grown film. Boron is a group III element and Sn is a group IV element, so that B on the Sn site should act as an acceptor. The boron impurities therefore compensate the film and increase its resistance. The increase in resistance observed after vacuum annealing may also occur because of F out-diffusion. Hence, we subsequently abandoned post-deposition annealing.

To block substrate interactions, such as the compensating diffusion of B into the films, borofloat glass substrates were subsequently coated with Al_2O_3 before growth of FTO. The SPEED deposited thin layer of Al_2O_3, using our existing recipe [60], acts as an impurity diffusion barrier. This function is inferred from the success in obtaining low resistivity SnO_2 film compared to when bare borofloat glass was used.

4.4.1 Scanning Electron Microscopy (SEM)

All deposited films grown at 440 ^{o}C and above appear uniform and shiny. Scanning electron microscopy (SEM) images were obtained using a Zeiss Ultra 55 SEM at 5 kV to characterize the particle morphologies. Figure 20 presents an SEM micrograph of an FTO film grown by SPEED at 460 ^{o}C. The SEM image reveals a dense nanostructure apparently devoid of cracks and voids. Grains of all FTO samples have about 100 nm lateral dimensions.
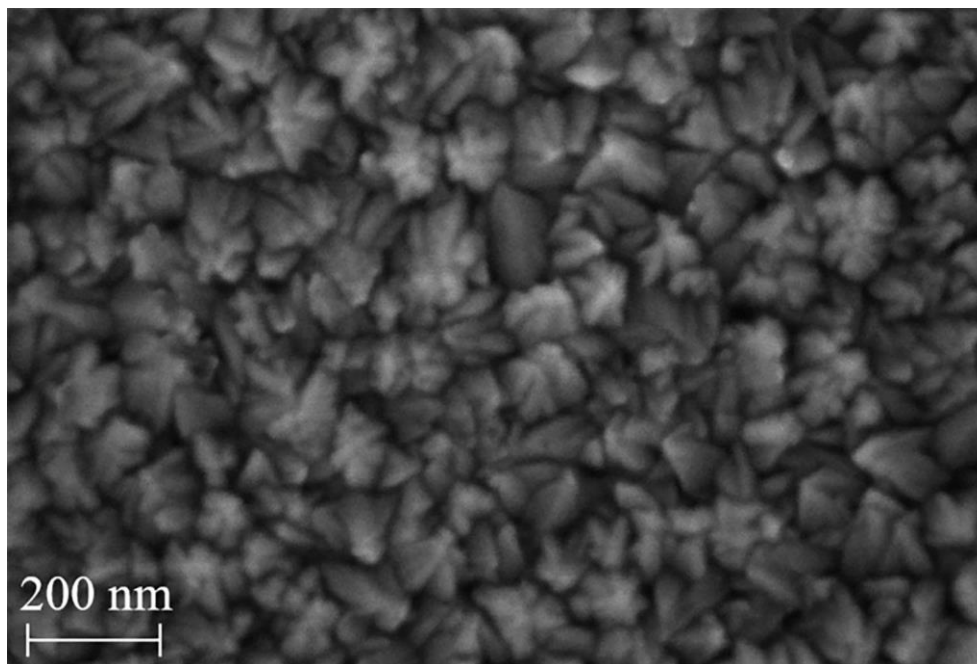
Figure 20 SEM image of FTO film grown on borofloat glass by SPEED at 460 ℃.

Cross-sectional SEM images were used to determine the thickness of FTO films. Figure 21 presents such images where both Al_2O_3 and SnO_2:F layers are evident despite charging of the glass substrate. Their thicknesses in this sample are approximately 150 and 250 nm, respectively. The top down and cross-sectional views (Figures 20 and 21, respectively) show that the film has a columnar growth. Thus the OH⁻ attachment for a subsequent molecule formation preferably takes place on an existing grain as explained in section 3.2.
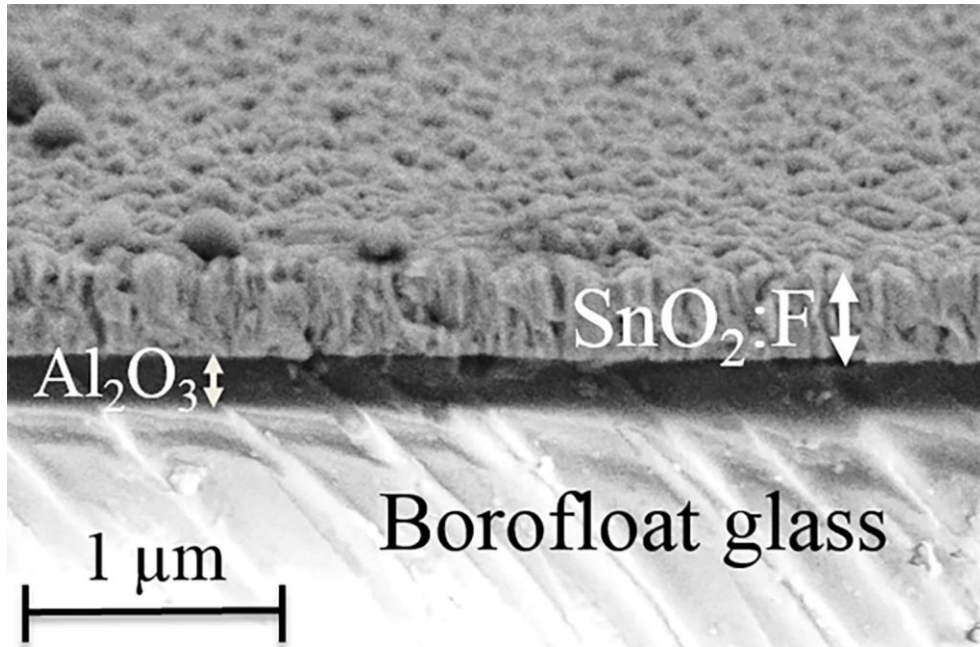
Figure 21 SEM cross section of FTO film grown on Al_2O_3 coated glass substrate.

4.4.2 Atomic Force Microscopy (AFM)

Atomic force microscopy (AFM) was performed by a Dimension 5000 AFM (Digital Instruments) in a contact mode for a 2.5×2.5 μm^2 array to study surface topology.

Figure 22 presents the surface morphology of an FTO film determined by Atomic Force Microscopy (AFM). The relief is at least 50- 70 nm, where the measurement is limited by the ability of the AFM tip to probe deep narrow recesses. This large area view of the film confirms the surface quality of the SPEED grown film. Here, the surface roughness is about the size of the grains constituting the film.
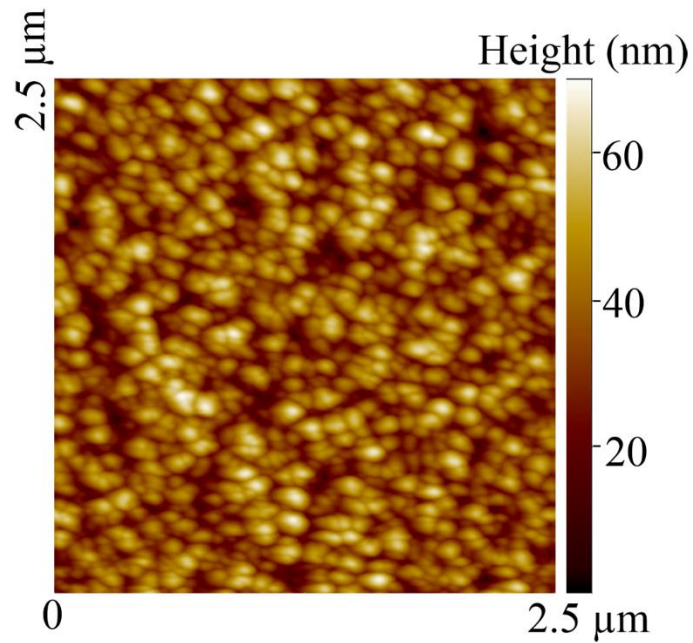
Figure 22 AFM image of the FTO film grown at substrate temperature of 460 °C.

4.4.3 X-ray diffraction (XRD)

A Panalytical Empyrean X-ray diffraction (XRD) system in asymmetric out-of-plane geometry (with 30 kV, 40 mA, Cu K_α radiation at $\lambda = 0.1540598$ nm) was used to record the XRD pattern of fabricated films for 2θ values from 20 to 80 degrees. The incidence angle measured with respect to the substrate plane was $\alpha = 15$ deg.

Figure 23 presents XRD 2θ-measurement for a FTO film, where reflections from (110), (200), (211), (310) and (301) planes of tetragonal SnO_2 [64] are observed. No peaks of any other crystal or phase are observed.
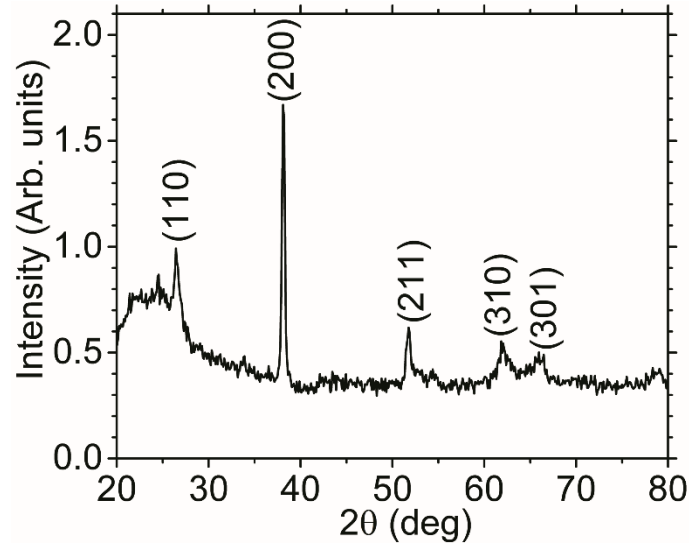
Figure 23 XRD spectra of FTO film grown at substrate temperature of 460 °C.

4.4.4 Normal incidence transmission with spectrophotometer

A Perkin-Elmer Lambda 900 spectrophotometer collected transmittance spectra T over the wavelength range 200 – 1000 nm. An Al_2O_3-coated borofloat glass was used in the reference beam. Absorption coefficient was calculated according to Beer's law, $\alpha = (1/d)\ln(1/T)$. Film thickness d was determined from cross-sectional SEM. The optical bandgap of the material was deduced from the absorption coefficient spectrum.

Figure 24 presents an unpolarized, normal-incidence transmittance spectrum collected at room temperature for a typical SPEED-grown FTO film in the wavelength range 250 to 1000 nm. The film microstructure (~100 nm according to Figures 20 and 22) is smaller than the wavelength, so that little scattering is expected. FTO film exhibits average transmittance of 93% in the visible range, and there is a sharp short-wavelength cut-off due to fundamental absorption [55]. These observations are in good agreement with the earlier reports for FTO [65-73].
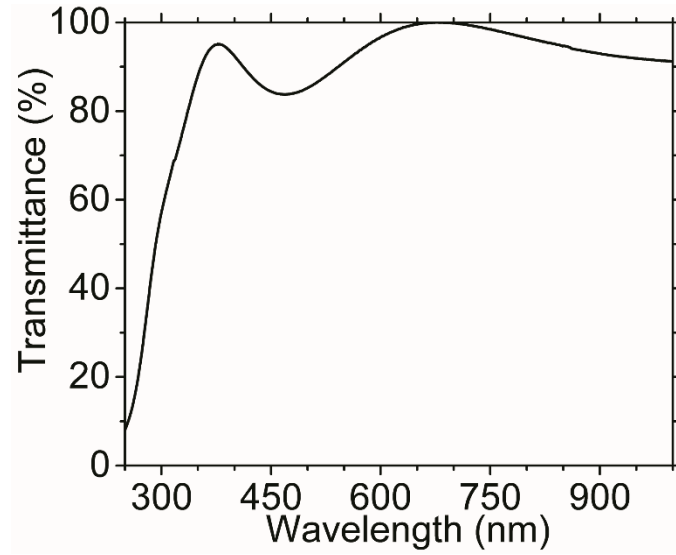
Figure 24 Transmittance spectrum of a typical SPEED-grown SnO$_2$: F film deposited on Al$_2$O$_3$-coated glass. Al$_2$O$_3$ coated glass was used as a reference during the data acquisition.

The absorption coefficient α is related to the incident photon energy by

$$\alpha h\nu = C(h\nu - E_g)^{1/2} \tag{6}$$

where C is a constant characteristic of the medium, E_g is the direct bandgap energy, hν is the photon energy [74]. By plotting $(\alpha h\nu)^2$ vs hν and extrapolating the linear portion to zero, we obtain the bandgap, as shown in Figure 25. The bandgap values of all films are around 4.0 eV. This value is in agreement with previous reports that the bandgap of FTO is in the range 3.9- 4.6 eV [52]. : The bandgaps of Al$_2$O$_3$ and the glass substrate are significantly larger, so that they do not contribute to the absorption in Figure 25.
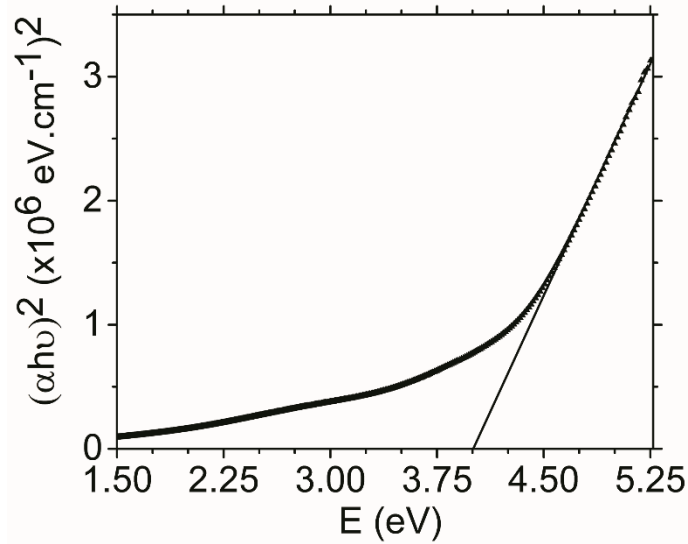
Figure 25 Plot of $(\alpha h\nu)^2$ as a function of photon energy (hν) has been used to estimate the optical bandgap of SPEED grown FTO thin-film.

4.4.5 Hall measurement

Resistivity, mobility, and carrier concentration were evaluated by Hall effect measurements at room temperature in a Van der Pauw four-point probe configuration, using indium contacts, in a Hall effect system (MMR technologies) with a magnetic induction of 0.65 T.

The Hall coefficients are negative for all films, confirming their n-type conductivity. The best results achieved for the 250 nm thick film are an electrical resistivity of 6×10^{-4} Ω.cm, Hall mobility 8.3 cm^2/V.s, and carrier concentration 1×10^{21} cm^{-3}. These values are comparable to most of the earlier reports for FTOs fabricated from SnCl$_2$ [65, 67-69] and SnCl$_4$ precursors [66, 71-73].

Haacke's figure of merit [75] for the photovoltaic application of transparent conducting films is $\varphi = T^{10}/R_s$, where T is the transmittance in the visible range and R_s is the sheet resistance. FTO film grown by SPEED method at 460 °C has a sheet resistance of 21 Ω/sq with average

transmittance of 93% in the visible range, which leads to $\varphi = 0.023$ S. This is comparable to numbers reported for FTO films fabricated by spray deposition [52, 75]. The value 0.071 obtained for sputter-coated TCO Cd_2SnO_4 is one of the highest known [75], and experimental FTO films grown by CVD have reached that value [52]. However, most commercial ITO and FTO coated glasses have values in the range 0.0009 to 0.020, and our FTO film is superior to these. The spray-pyrolysis-grown FTO sample with the same thickness as ours of Ref. [52] had the lower value 0.018, since our sample has higher transmittance and comparable sheet resistance relative to that sample.

CHAPTER FIVE: PLASMON POLARITONS IN FLOURINE DOPED TIN OXIDES IN INFRARED

5.1 Introduction

The motivation of this work has been finding plasmonic host materials that are efficient in IR region of the spectrum. Heavily-doped degenerate semiconductors, such as indium tin oxide (ITO), aluminum doped zinc-oxide (AZO) and gallium-doped zinc oxide (GZO) are some examples of transparent conductor oxides (TCOs) and have been recently studied for applications in nano-photonics [28, 76]. Moreover, it has been shown that the carrier density and the permittivity of TCOs can be tuned in a broad range by applying an external electric field [77].

SPPs at the telecom wavelength and higher wavelengths in IR could be supported by TCOs due to their high concentration of free carriers and consequently, relatively high plasma frequency. ITO is the most well-known of TCOs with a plasma frequency in the near-IR region, making the material to be reflective in the mid-IR.

Experimental and theoretical investigations of plasmonic properties of TCOs is mostly focused on ITO [76-80] while the literature in fluorine-doped tin oxide is still behind. Thus, our focus here is investigating the plasmon polaritons in FTO for their potential in IR plasmonics.

5.2 Optical properties of FTO thin films

Fluorine doped tin oxide with 20% fluorine dopant relative to tin was fabricated directly on borofloat glass. The thickness of the film was conformed to be around 200 nm with SEM. The transmittance $T(\lambda)$ and reflectance $R(\lambda)$ spectra of the FTO sample fabricated by SPEED have been recorded in Figure 26 from 600 nm to 8 microns. By having the accurate thickness of FTO film, complex permittivity values of FTO can be calculated.
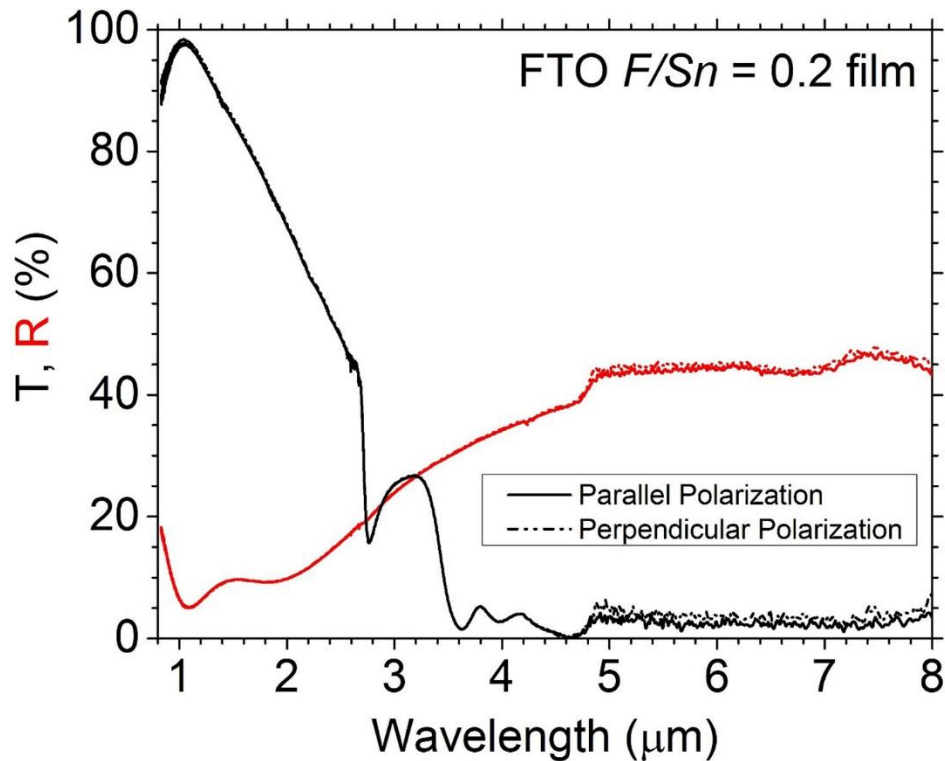
Figure 26 Transmittance and reflection spectrum of a FTO film grown on glass at 460 °C with 20% fluorine dopant level.

The drop in reflectance observed just below 3 microns is due to the low transmission from borosilicate glass substrate in this range.

5.3 Ellipsometry of fluorine-doped tin oxide thin-films

The FTO films were characterized by a J. A. Woollam IR-VASE ellipsometer, which spans the wavelength from 0.6 to 6 microns. Complex permittivity spectra of fabricated FTO thin films on glass is presented in Figure 27. First, an uncoated borofloat glass substrate and a substrate with

250 nm of FTO was measured. The Woollam WVASE32 software was used to determine the complex permittivity of FTO grown by SPEED method at 460 ℃.
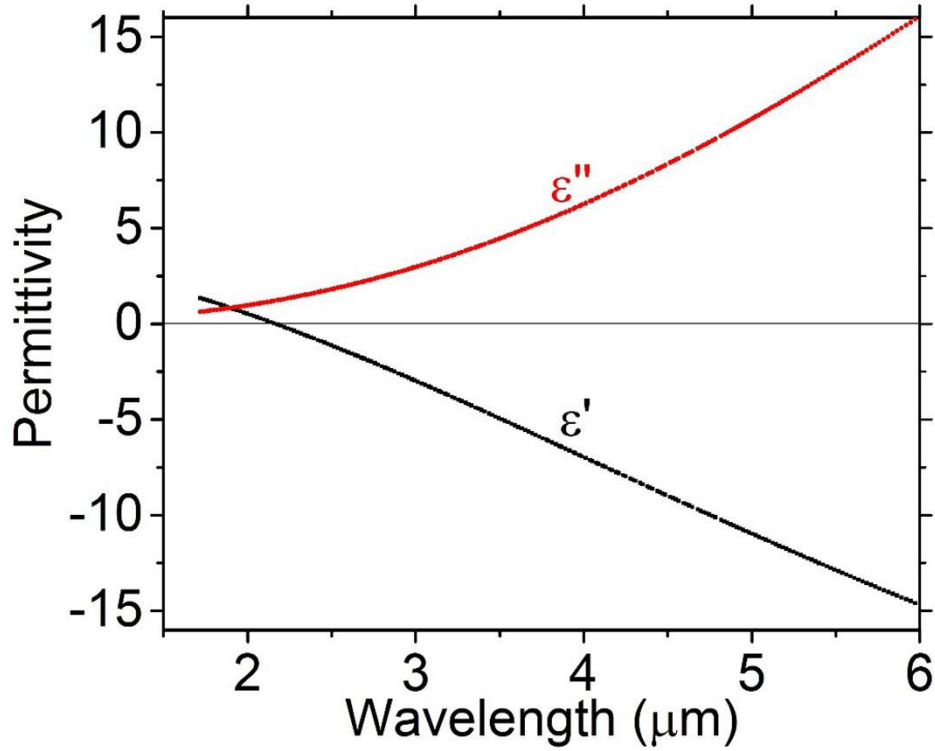
Figure 27 Complex permittivity of a FTO thin films grown on glass in range of 1-6 microns.

From Figure 27 it is clear that real part of permittivity crosses zero at 2.16 μm (screened plasma frequency) and real and imaginary parts of permittivity are equal at 1.89 microns. The Drude free-electron model was used to fit the Drude parameters to the ellipsometry measurements in NIR-MIR. The Drude fit results to 284.5 THz for **surface plasma frequency (ω_{sp})**, 43.28 THz for Γ and 3.853 for the real part of permittivity well above plasma frequency which is in agreement with earlier report from Dominici et al. [81].

Nobel metals such as Ag and Au are not suitable for plasmonic applications at NIR-MIR because of extremely low compactness at these wavelengths [28]. On the other hand, wide-bandgap semiconductors such as ITO and FTO could be efficient nanoplasmonic hosts due to their strong confinement of SPPs and low loss.

5.4 Fabrication of lamellar gratings of fluorine-doped tin oxide

Si lamellar grating were fabricated with a photomask with 4 different periods of 7.5, 15, 10 and 20 microns and 50% duty cycle. Si grating couplers were photolithographically patterned by deep reactive ion etching (DRIE) using a STS DRIE system. An optimized process with combination of C_4F_8, SF_6, CF_4 and O_2 gases which uses a two-step etching/passivation step, was successfully developed. The resulting gratings possess straight sidewalls and could be manufactured with various amplitudes. A thin layer SiO_2 then was deposited onto the Si gratings by plasma enhanced chemical vapor deposition (PECVD) in order to make the substrate grating hydrophilic and ready for the SPEED coating of lamellar Si gratings.

Here, we focus on gratings with amplitude of 1 to 1.5 microns. A uniform FTO coating then was deposited on all Si grating using the SPEED method. Figure 28 shows a top view of a Si grating with $p = 7.5$ μm, 50% duty cycle and 1.5 μm amplitude (FTO-NN-G5) that was coated by a FTO film at temperature of 460 ºC .
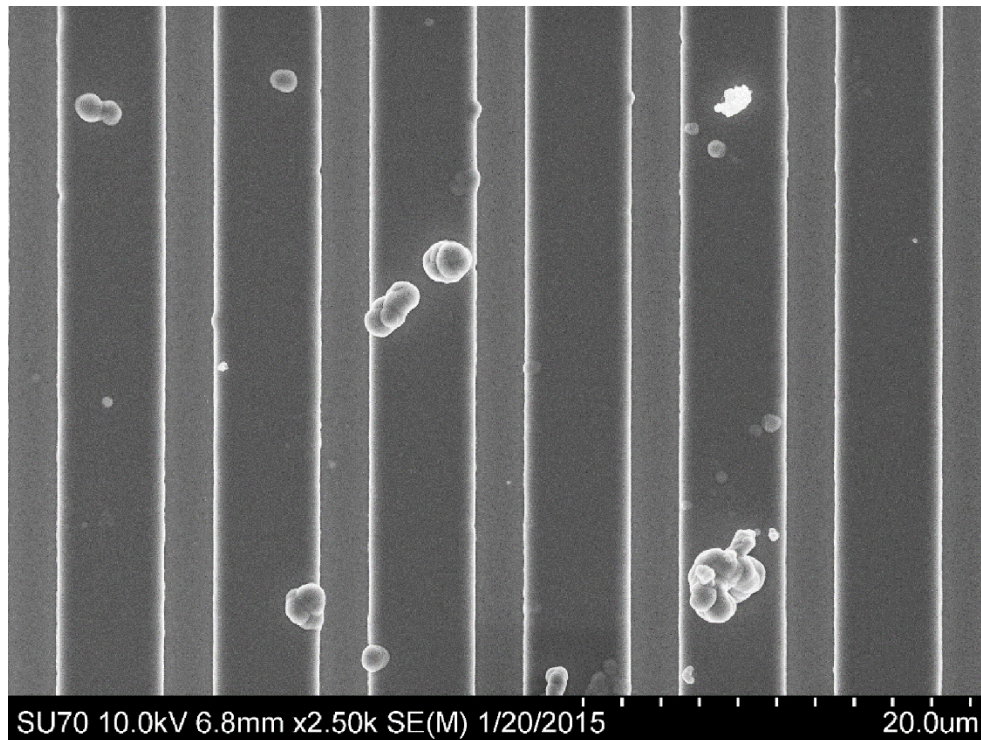
Figure 28 SEM top veiw of FTO gratings with period of 20 microns.

The FTO-G1 grating then was cleaved and polished by a mechanical polisher. The SEM cross section of the FTO-G1 grating then was taken buy a Zeiss Ultra 55 system at 5 kV and with working distance of 2.5 mm. The depth of grating G1 was around 1.46 μm while the FTO coating deposited by speed varied from 560 to 590 nm. Each grating bar's length is found to be around 4.9 μm form Figure 29.
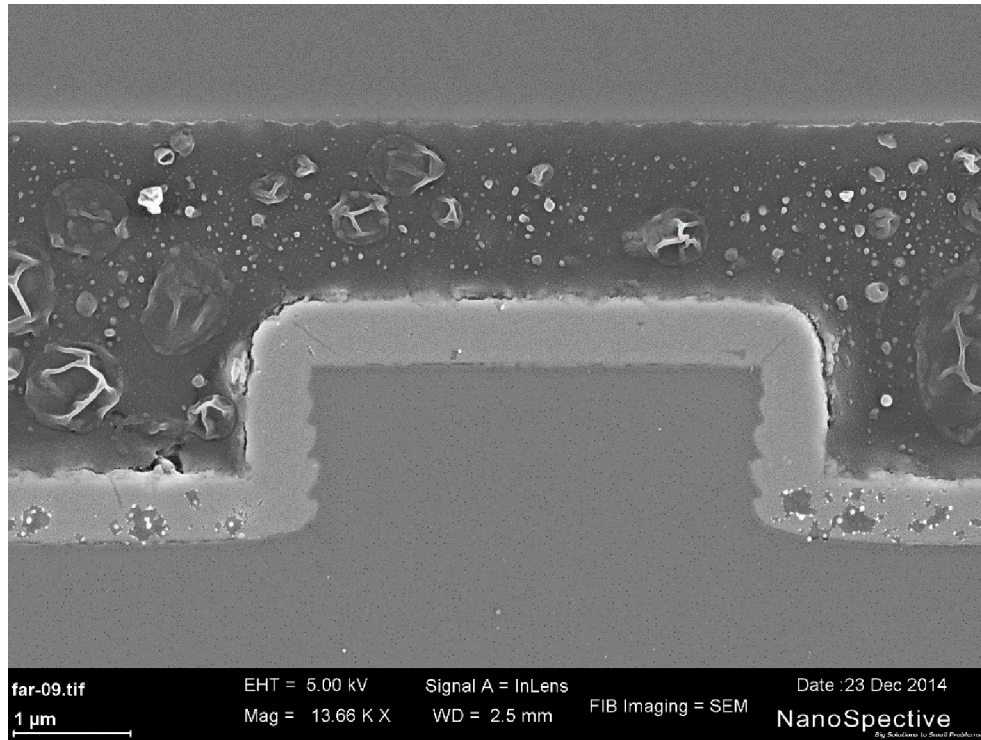
Figure 29 SEM cross section of polsihded FTO gratings deposited on Si. Two layers of Si ans FTO are disticnt with an adhesive layer attahcing sample to wafer handle seen on top.

A second set of grating with $p = 20$ µm and 50% duty cycle were also fabricated on Si and coated by a FTO layer. Amplitude of these gratings were measured by profilometry to be around 1.6 microns as it is shown in Figure 30.
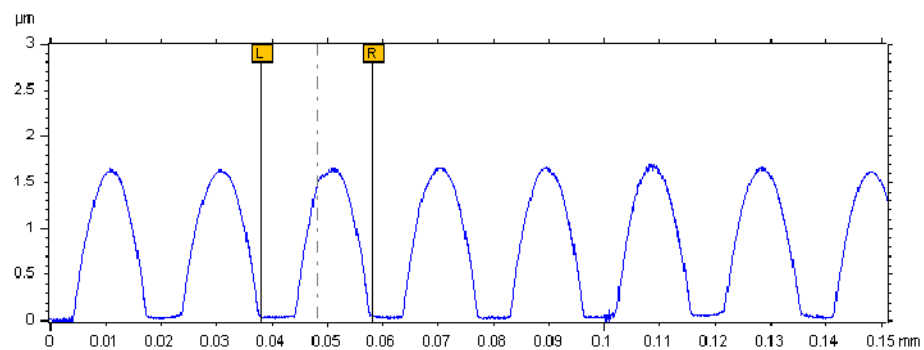
Figure 30 Height profile of FTO grating (NN3) shows an average amplitude of around 1.6 microns.

5.5 FOURIER TRANSFORM INFRA-RED (FTIR) reflectance of FTO gratings

FTIR reflectance spectra of FTO gratings were acquired by a FTR microscope at normal-incidence. 0 deg polarization corresponds to p- (TM) polarized light while 90 deg polarization represents the s- or TE polarization. The surface plasmon polaritons are expected to be excited for TM polarization when the incident light's propagation is along gratings groove and polarization is perpendicular to grating grooves.

Figure 31 shows the calculated n_{spp} values from ellipsometry measurements plotted together with different grating modes, or when the value of $Sin\theta + (2\pi/\lambda)m$ equals to the k_{spp} (this can be called the resonance condition). For a normal incidence at 0 deg, 3 possible modes of m = -3, -2, -1 could be observed at different wavelengths in MIR as it is shown in Figure 31.
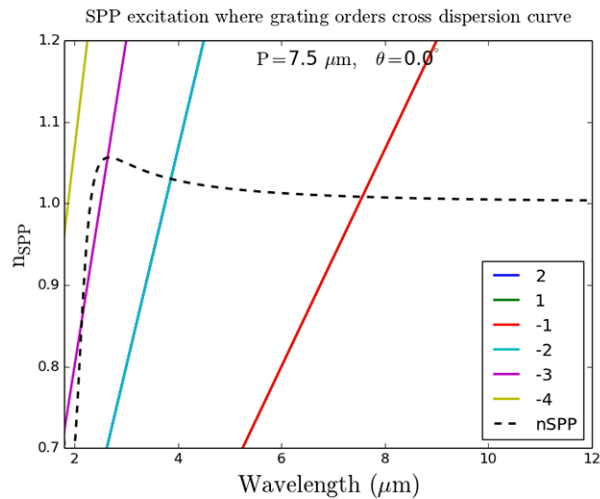
Figure 31 Possible excited SPP modes for a FTO grating with period of 7.5 microns at normal incidence.

According to Figure 32, the FTIR reflection spectrum of a grating with p = 7.5 μm shows a dip around 8 μm for a TM incident light which could correspond to the m = -1 resonance mode.

There is also a minor dip observed at 3.8 microns of TM mode that can be possibly related to the

m = -2 mode.
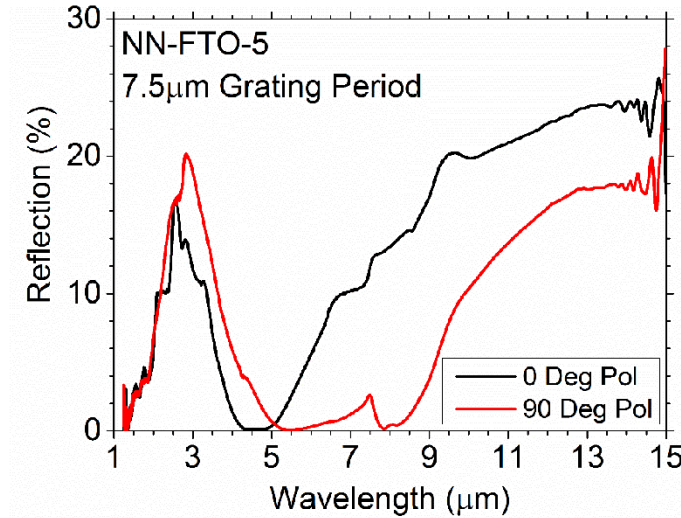
Figure 32 FTIR reflectnace of FTO coated Si grating with period of 7.5 microns.

Figure 33 shows the calculated n_{spp} values from ellipsometry measurements plotted together with different grating modes, or the resonance condition. For a normal incidence at 0 deg, 4 possible modes of m = -4, -3, -2, -1 could be observed at different wavelengths in IR as it is shown in Figure 33.
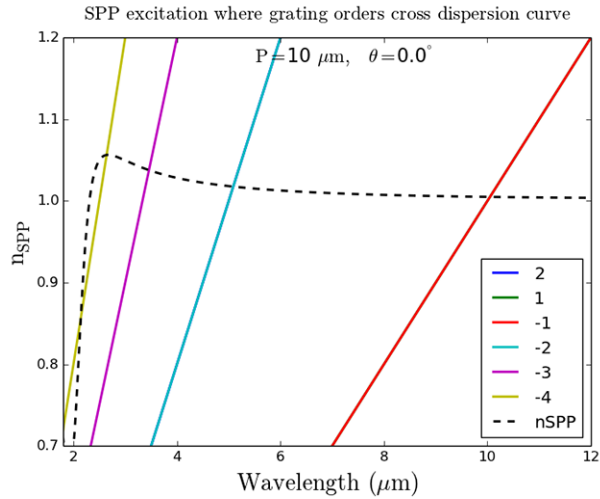
Figure 33 Possible excited SPP modes for a FTO grating with period of 10 microns at normal incidence.

Figure 34 shows the FTIR normal incidence reflectance for a FTO grating with $p = 10$ μm. Two resonances are observed for p-polarized light (90 deg polarization): a strong dip just below 10.5 μm which corresponds to m = -3 mode.
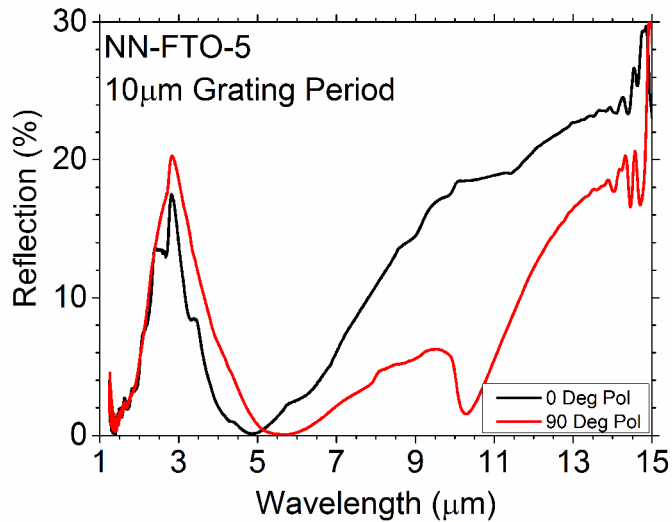
Figure 34 FTIR reflectnace of FTO coated Si grating with period of 10 microns.

Figure 35 shows the predated resonances in reflectance for a FTO grating with $p = 20$ μm grating. Three resonances are predicted for p-polarized light (90 deg polarization) at wavelength from 4 to 10 microns.
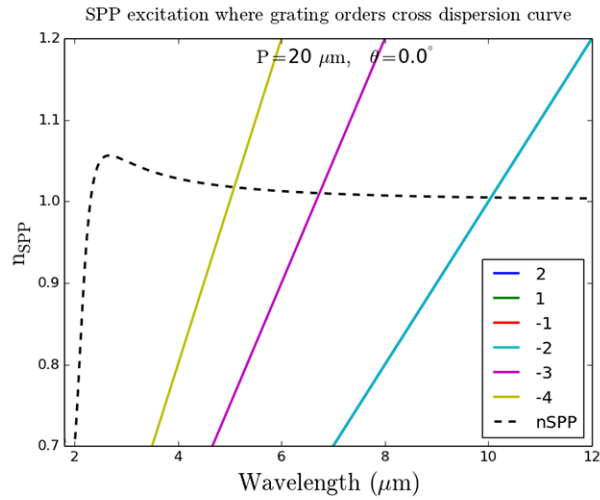
Figure 35 Possible excited SPP modes for a FTO grating with period of 20 microns at normal incidence.

Figure 36 shows the FTIR reflection spectra of a FTO grating with 20 microns period with a major dip in reflection spectra of a TM-polarized light just below 7 μm, which could correspond to m = -3 mode.
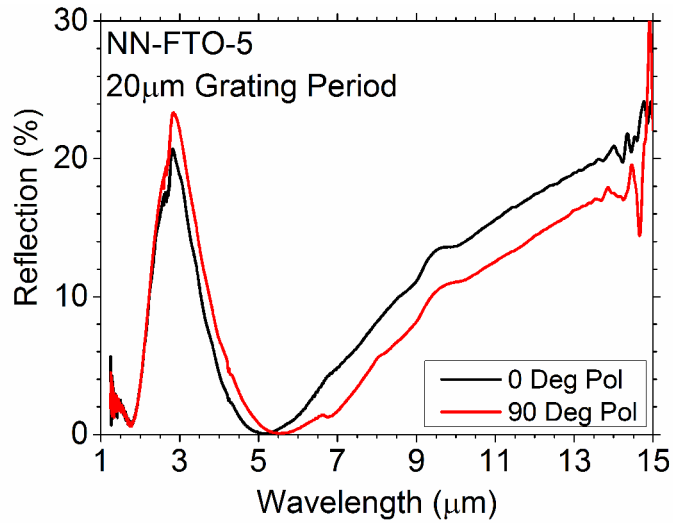
Figure 36 FTIR reflectnace of FTO coated Si grating with period of 20 microns.

5.6 Angular and specular reflectance measurements of FTO gratings couplers

5.6.1 Angular and specular reflectance of a FTO grating-G1with p = 7.5 μm

The reflectance of the FTO grating was measured using a tunable quantum cascade laser (QCL) from Daylight solutions with specular resolution of 0.1 nm. The incident radiation was tunable in the range of 7.9 μm to 10.5 μm, and was digitally chopped at 1 kHz. A mercury cadmium telluride (MCT) detector was used to measure the reflected intensity, utilizing a lock in amplifier to demodulate the signal at the chopping frequency. With the QCL fixed, the sample and detector were rotated to perform angular reflectance measurements. For the specular reflectance measurements, the angle of incidence is fixes and the wavelength is swept from 8 to 10.5 microns in 0.25 microns increments.

Figure 37 represents the angular reflectance of a FTO grating with period of 7.5 microns in various frequencies in mid-IR. A broad resonance corresponding to m = -1 mode is observed

for all wavelengths. By increasing wavelengths, the angular resonance shifts toward higher angles on incidence. All angular shifts can be explained by changes in SPP dispersion curve toward higher wavevector values. It is seen in Figure 37 that for lower frequencies in IR, the resonance angle shifts toward the larger angles due to increase in the value of the wavevector.
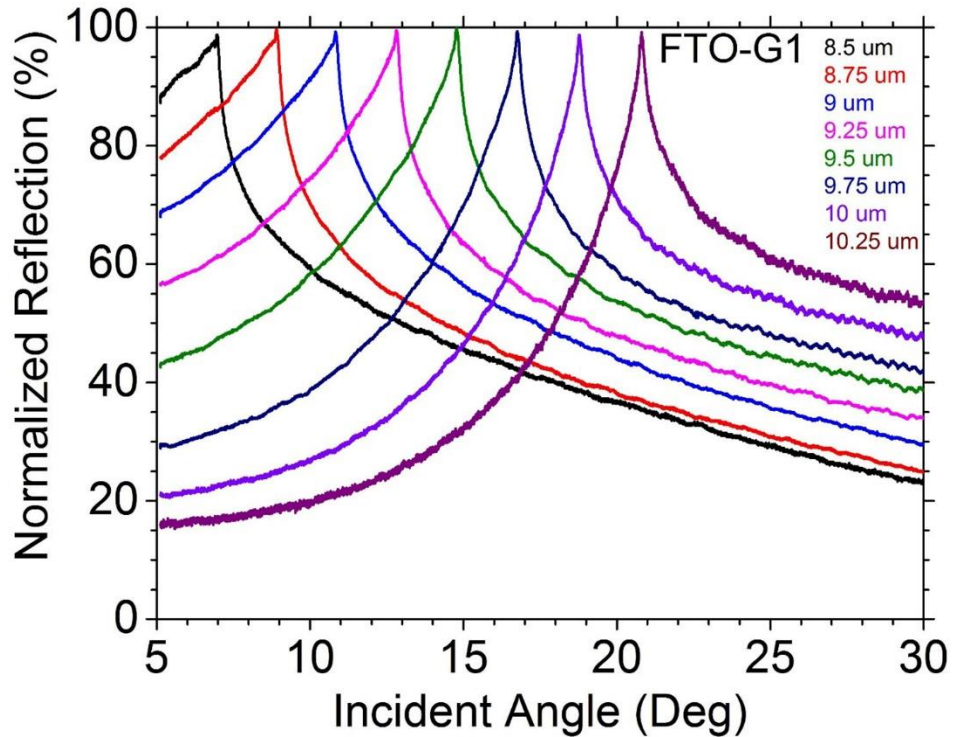
Figure 37 Angular reflectance spectra for FTO gratings with p = 7.5 μm at 8 different wavelengths from 8.5 to 10.25 microns corresponding to the m = -1 resonance mode.

Figure 38 (below) shows the specular reflectance of a FTO-G1 grating with $p = 7.5$ microns for nine different incident angles ranging 6 to 22 deg in 2 deg increments, while the laser wavelength is swept from 8 to 10.5 microns. . Lineshape and depth of each resonance depends on height and profile of the grating grooves. The m = -1 resonance is observed in specular reflectance graph when the decreasing k_{spp} value results in lower θ_{res}. Other resonance modes (including m =

-2, -3, +1) are expected to be observed in 2-6 micron range in mid-IR which lies outside of our laser range.
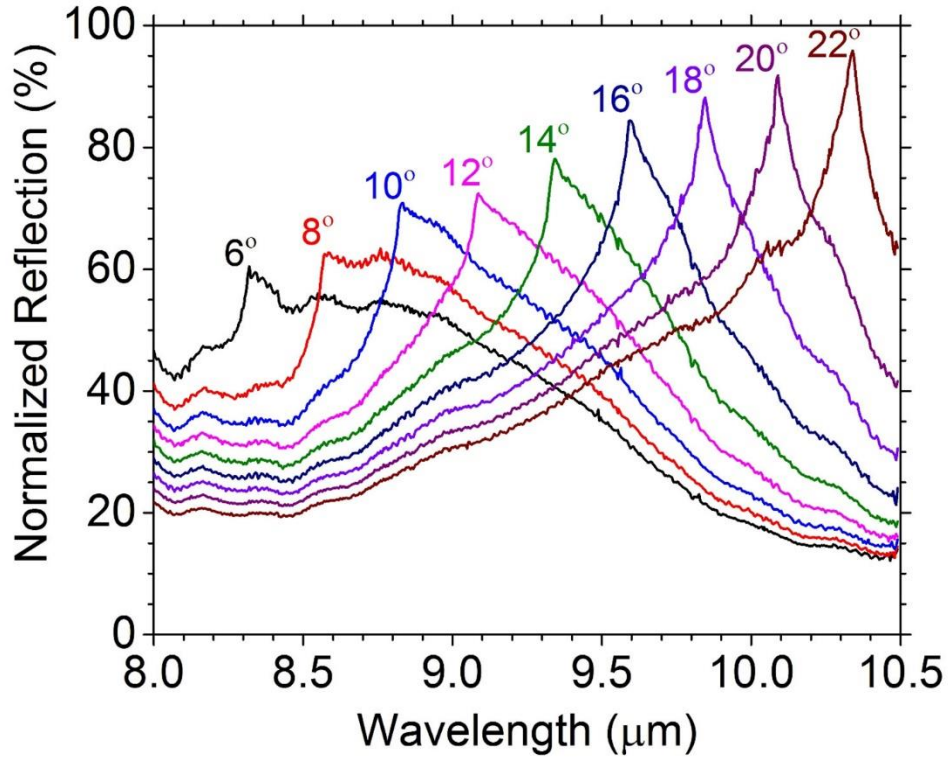
Figure 38 Specular reflectance spectra for lamellar FTO gratings at different incidence angles corresponding to the m = -1 resonance.

5.6.2 Angular reflectance of a FTO grating with p = 20 μm

Figure 39 shows the angular reflectance spectra of a 20 μm grating in increments of 0.25 microns from 8 to 10.5 microns. There are two diffracted modes observed: m = -3 and m = +1. In m= +1 mode, increasing the laser wavelength will result the angular resonance to shift to lowers angles while for m = -3 mode, the resonances shift toward higher angles with increasing (QCL) wavelength.
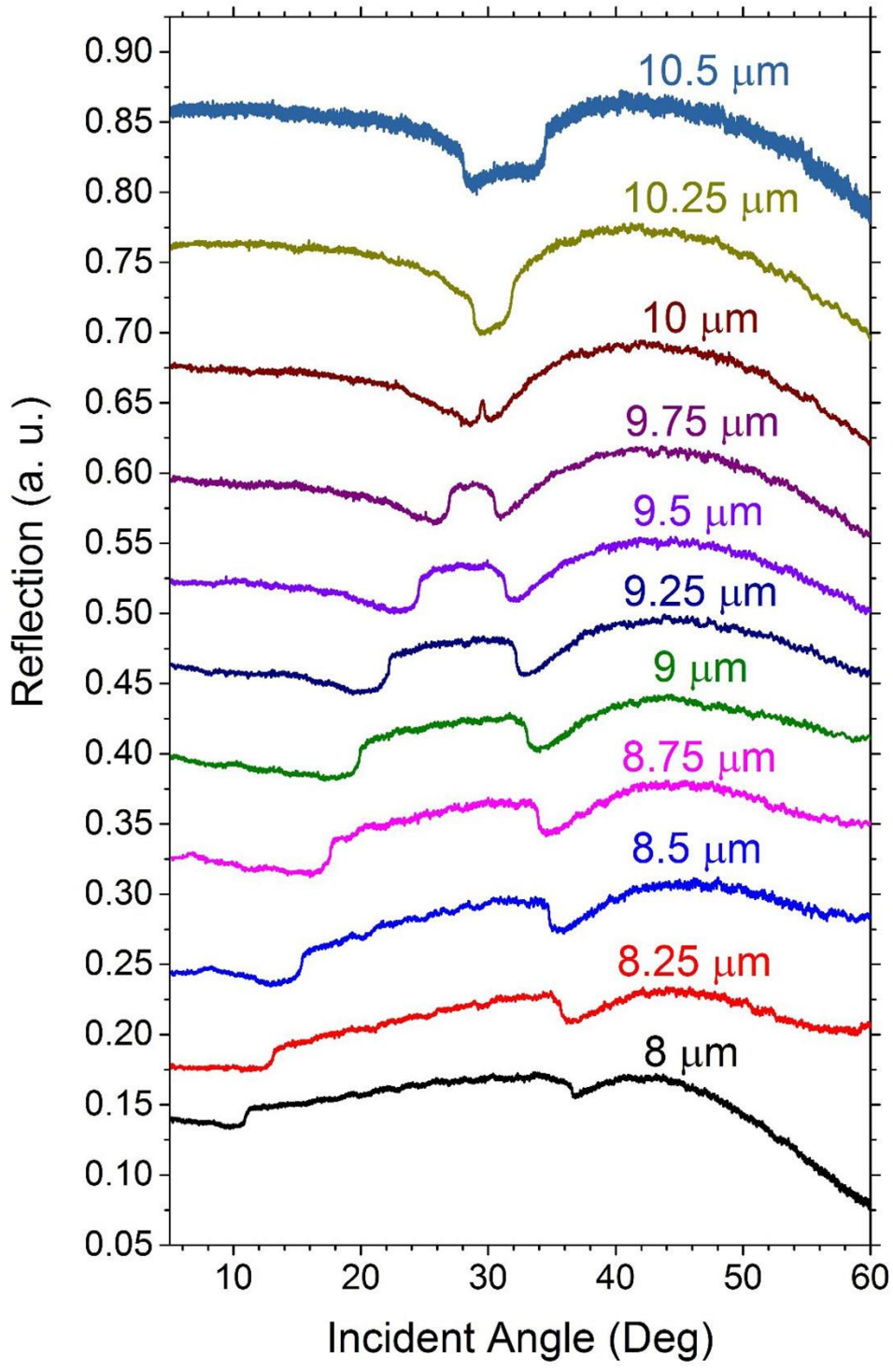
Figure 39 Angular reflectance spectra for FTO gratings with p = 20 μm at different wavelengths corresponding to the m = -3 and +1 resonance modes.

CHAPTER SIX: PLANAR INTEGERATED PLASMONIC MID-IR SPECTROMETER

6.1 Introduction

Here in this chapter we have investigated the integration of plasmonic elements with silicon photonics to provide a possible chip scale chemical sensor and spectrometer compatible with complementary metal-oxide semiconductor (CMOS) fabrication technology [22, 82]. Opportunity that we are looking for here is for a planar integrated spectrometer which uses a broadband IR source and is based on a Si photonic waveguide.

We present a compact mid-IR spectrometer based on a broad-band light source, dielectric waveguides, a transformer to convert between waveguide modes and surface plasmon polaritons (SPP), an interaction region where analyte molecules are interrogated by SPPs, an array of ring resonators to disperse the light into spectral components, and photodetectors.

A light source will emit into a dielectric waveguide, which will lead to a region which will allow coupling of the incident photons into SPPs. These will propagate along a functionalized metal surface within a sample interaction zone. This functionalized metal surface will allow interactions between the propagating SPP and any analytes bound to the surface, causing increased loss at those wavelengths that correspond to the analyte vibrational modes. After a suitable propagation length the SPP will be coupled back into a dielectric waveguide, where specific wavelength components will be out-coupled to detectors by an array of ring resonators. The simplest useful spectral sensor of this design would have two spectral channels. The use of SPPs in the interaction region favors application to surface.

6.2 Light emitting diode source in mid-IR

Infrared light emitting diodes (LED) offer smoother, broader, stable, cheaper solution with wavelengths in H stretch region. So, a set of these LEDs was purchased from Boston Electronics at the very attractive cost (in comparison to QCLs) of just ~$100 each. Their spectra (Figure 40) and temperature dependence were characterized using a Fourier transform infrared (FTIR) spectrometer of a Bomem DA8 with a KBr beam splitter using a 77 K-cooled InSb detector.

The LEDs were mounted at the spectrometer emission port. Each LED was operated at the specified maximum power conditions in continuous wave mode, with an excitation current of 100-200 mA. Each observed band matches the center wavelength specified. Shifts with temperature, measured by attaching the LED to a thermoelectric heater/cooler, were less than the emission bandwidths. Unlike the QCL, there is no mode structure. In comparison to QCLs, the range of available wavelengths is shifted to the blue, such that the important region of characteristic vibrations below 3 microns is accessible.

Normalized spectra of several of the LEDs are shown below in Figure 40. They span the range from approximately 1.9 to 7 microns and are much less expensive than QCLs, leading to the potential for very inexpensive systems in the near term.
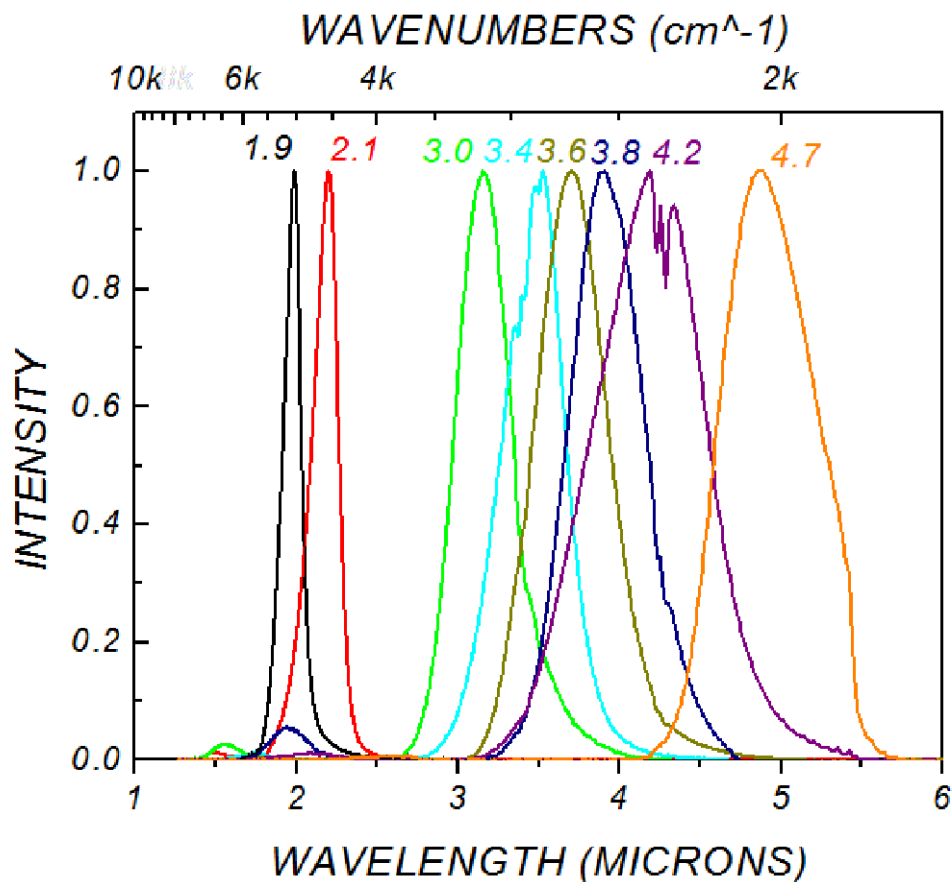
Figure 40 Normalized spectra of mid-IR LEDs obtained from Boston Electronics, measured with the Bomem FTIR spectrometer at UCF using a liquid nitrogen-cooled InSb detector.

We will work with the 3.4 micron (200 μW CW, 500 μW pulsed) LED for the rest of measurements. The wavelength region near 3.4 microns is very important not only because of the atmospheric transmission window between 3 and 5 μm, but because it is the C-H stretch region for all hydrocarbons as well as NH, OH, CO double bonds, NH_2, and CN. This region is hence especially important for identifying specific chemical and biological threats. The targeted short wave infrared SWIR region (3 - 4 μm wavelengths) features low loss propagation in silicon and the characteristic absorptions of (e.g.) C-H (Alkynes), O-H (monomeric alcohols, phenols), N-H (Amines), CO double bonds, NH_2, and CN, as shown in Figure 41. This motivates the shift to

longer wavelengths from telecom bands, where the first work waveguide-to-plasmon modes using tapered waveguides was done [83].
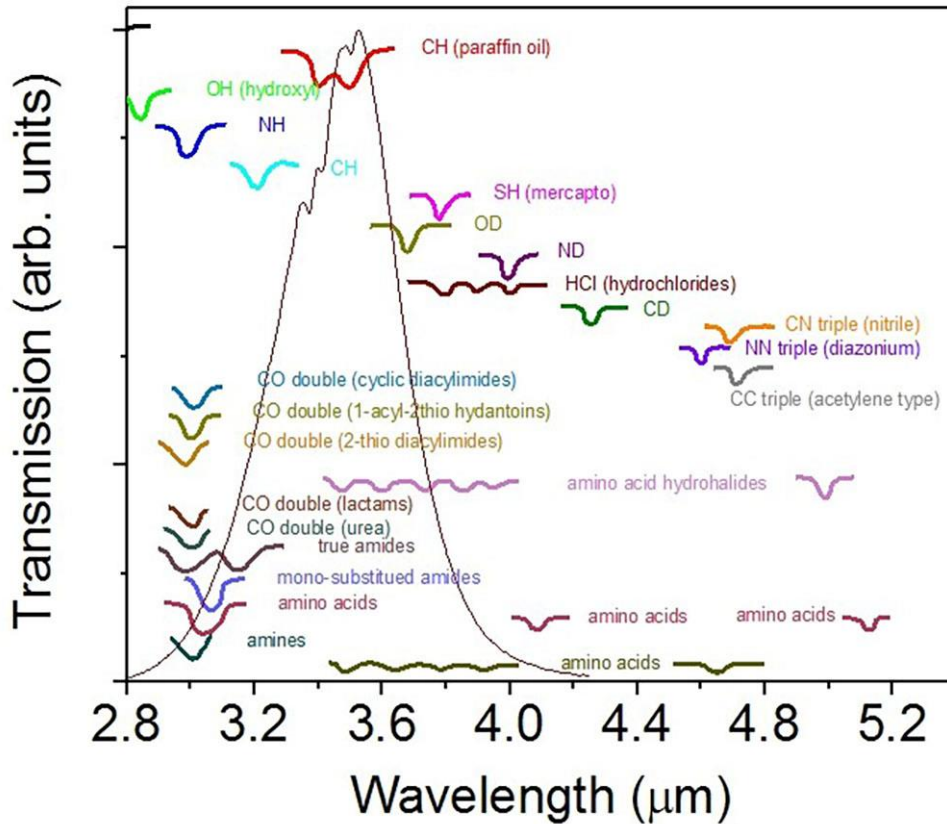
Figure 41 Representative spectra of molecules superimposed on the measured spectrum of a 3.4 μm LED.

Although proposed several years ago, the first experimentally verified transmission of mid-IR radiation through SOI waveguides was published only recently [84]. The authors coupled 3.39 μm radiation from a He-Ne laser into a bundle of single mode fibers which were end fire-coupled to their silicon-on-insulator (SOI) waveguides. The use of ring resonators as frequency selective elements has also been verified in the mid-IR suggesting their usefulness in this proposed application [85].

<u>6.3 Silicon waveguides for mid-IR applications</u>

6.3.1 Silicon on insulator (SOI) waveguides in mid-IR

A bent Silicon waveguide on a Silicon-on-insulator (SOI) platform has been designed to isolate the output light from the IR input. Figure 42 shows the schematic of a bent Si waveguide on a silicon oxide substrate. In order to eliminate the possibility of detecting LED light later in light-coupling, the design is based on a waveguide with 90 deg bend.
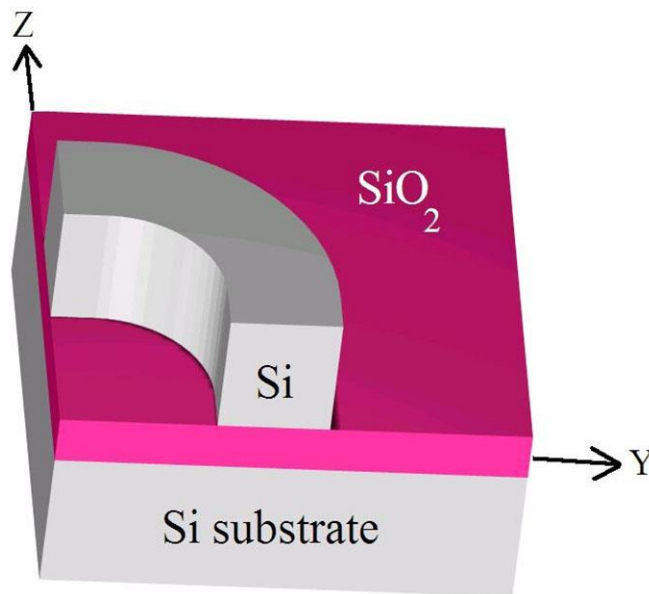
Figure 42 Schematic of the bent silicon on SOI platform.

The structure is based on a 10 micron wide x 10 micron tall Si waveguide on a SiO_2 slab. Initial propagation is assumed to be in $+z$-direction. After the 90 deg bend, the propagation mode will be rotated along $-y$ direction.

Lumerical FDTD solutions has been used to simulate the propagation mode in the proposed structure. Figure 43 presents results of 3D FDTD simulation that demonstrate the creation of

surface plasmons inside the SOI structure. The silicon waveguide has 10 μm x 10 μm cross section on oxide.
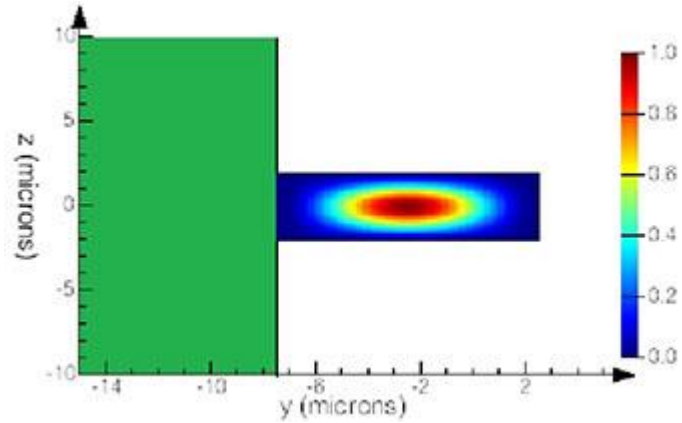
Figure 43 Schematic of the bent silicon waveguide establishing the coordinate system used in the electrodynamic simulations.

Our starting material is commercial SOI wafer (10 μm thick silicon on 10 μm oxide). SiO$_2$ has low loss at 3.4 microns. Structures are defined by conventional lift-off in Al, which serves as etch mask. Etching is performed in deep reactive ion etching (DRIE) using a STS RIE system. Figure 44 is an SEM image of waveguides on a SOI platform.
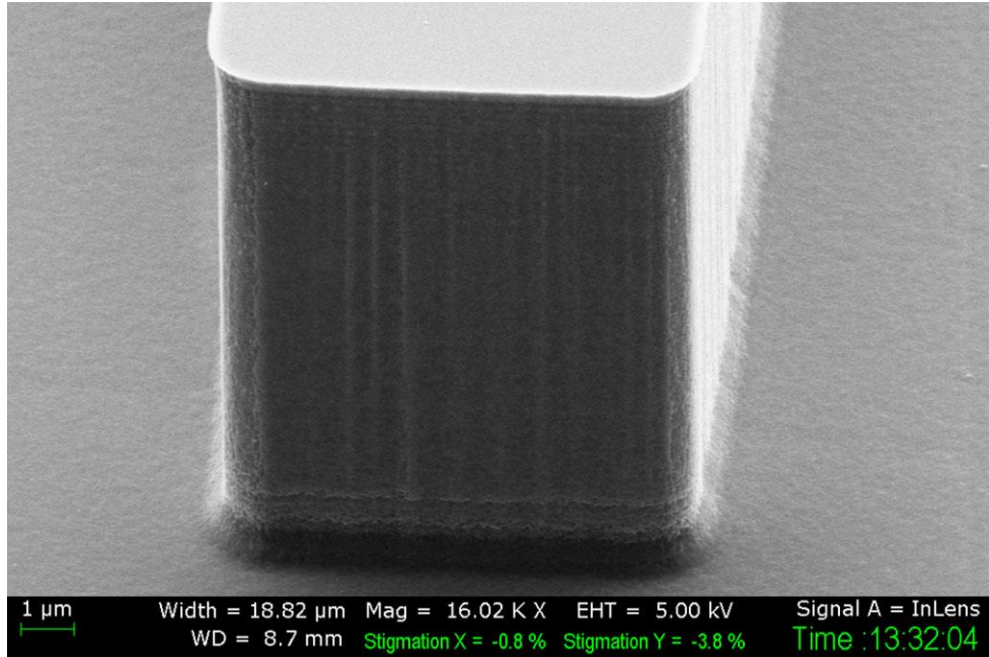
Figure 44 A Si waveguide has been fabricated photolithographically on a SOI platform..

6.3.2 Ring-resonator for high resolution spectroscopy

High resolution spectroscopy can be achieved by implanting cascade ring resonators. The optical resonance will occur when circumference of a micro-ring resonator is equal to integral (m) number of signals wavelengths λ/n in, where n is the refractive index of Si and λ is the vacuum wavelength. For hypothetical photons of 3.4 micron wavelength travelling through silicon (n = 3.4), the circumference must therefore be m microns. Figure 45 presents a schematic of set of ring resonators.
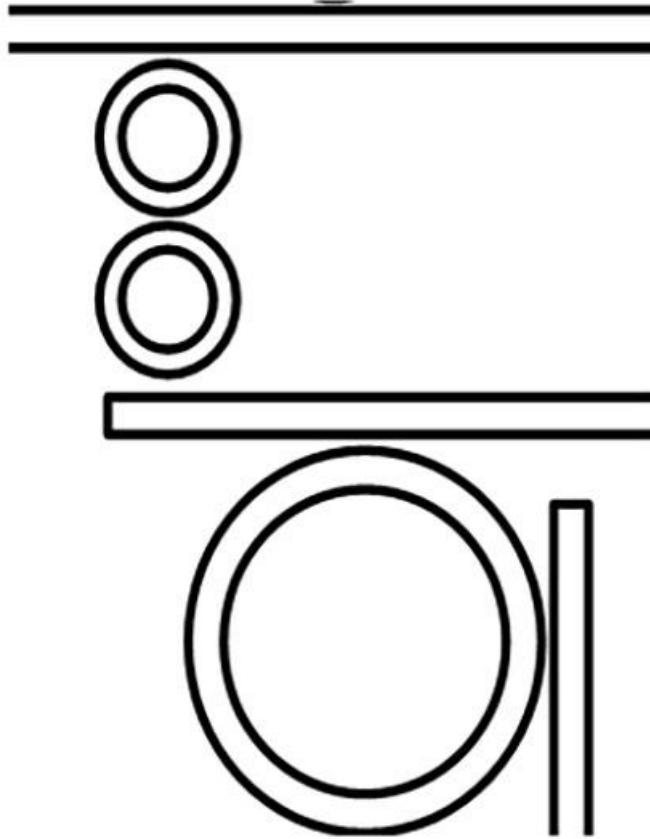
Figure 45 Set of ring resonators could be used for high resolution spectroscopy.

The resolving power (Q) of the micro-ring resonator is dependent on its width, as a large width can allow transverse modes. We desire a $Q = \lambda/\Delta\lambda$ of at least 1000 to ensure that each ring will act as single resolution channel with a reasonably useful resolution of $\Delta\lambda = 3$ nm. This value of Q seems readily obtainable with present fabrication techniques. The precise requirements of the micro-ring resonator's circumference and width may be achieved in principle by photolithography. The device may be conveniently fabricated from silicon-on-insulator (SOI), where the waveguides and rings are supported by a layer of SiO_2, which has lower index than silicon. Figure 46 presents a 3-micron wide Si micro-ring resonator fabricated on an oxide layer by deep reactive ion etching (DRIE).
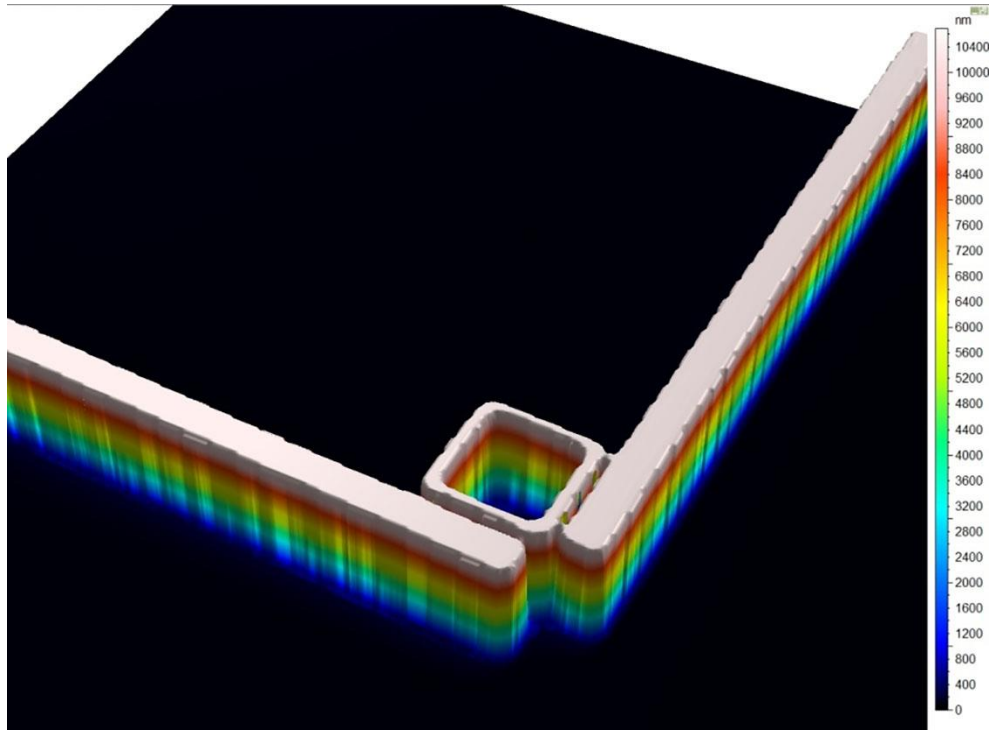
Figure 46 A sample 3 micron-wide resonator has been fabricated by DRIE.

As an example to understand how set of micro-ring resonators can work to resolve the spectrum of a broad light source, let's consider our proposed LEDs spectrum at 3.4 microns where its bandwidth is ~ 400 nm. A first layer of micro-ring resonators with 1.58 μm diameters might be used to resolve part of the broad LED spectrum around 3.38 μm. With introducing second set of ring resonator with 15.82 μm diameter, the resonance full width at half maximum (FWHM) of around 3 nm could be achieved. More sets of ring resonators with the right optical path lengths, will be added in the same manner to achieve the desirable resolution at each wavelength between 3.3 to 3.5 μm.

6.4 Mid-IR spectrometer design and parameters

Figure 47 presents a design schematic consisting of source, interaction, and detector regions. A commercial 3.4 μm wavelength LED with ~ 400 nm bandwidth is proposed for use as the optical source which will be coupled into a silicon-on-insulator waveguide adiabatically tapered to a dimension below cutoff, in order to transform the waveguide mode to a plasmon that propagates in the metallic slot of the interaction region shown schematically in Figure 47 (b). Molecules will interact with the bound electromagnetic waves in this region, giving rise to absorption. Functionalizing the surface in the interaction region will allow concentration of the molecular analyte in order to measure the infrared absorption of the bound molecules as well as to probe their binding kinetics. After conversion back to a waveguide mode via another adiabatic taper, wavelength dispersion is accomplished through the use of a series of micro-ring resonators.
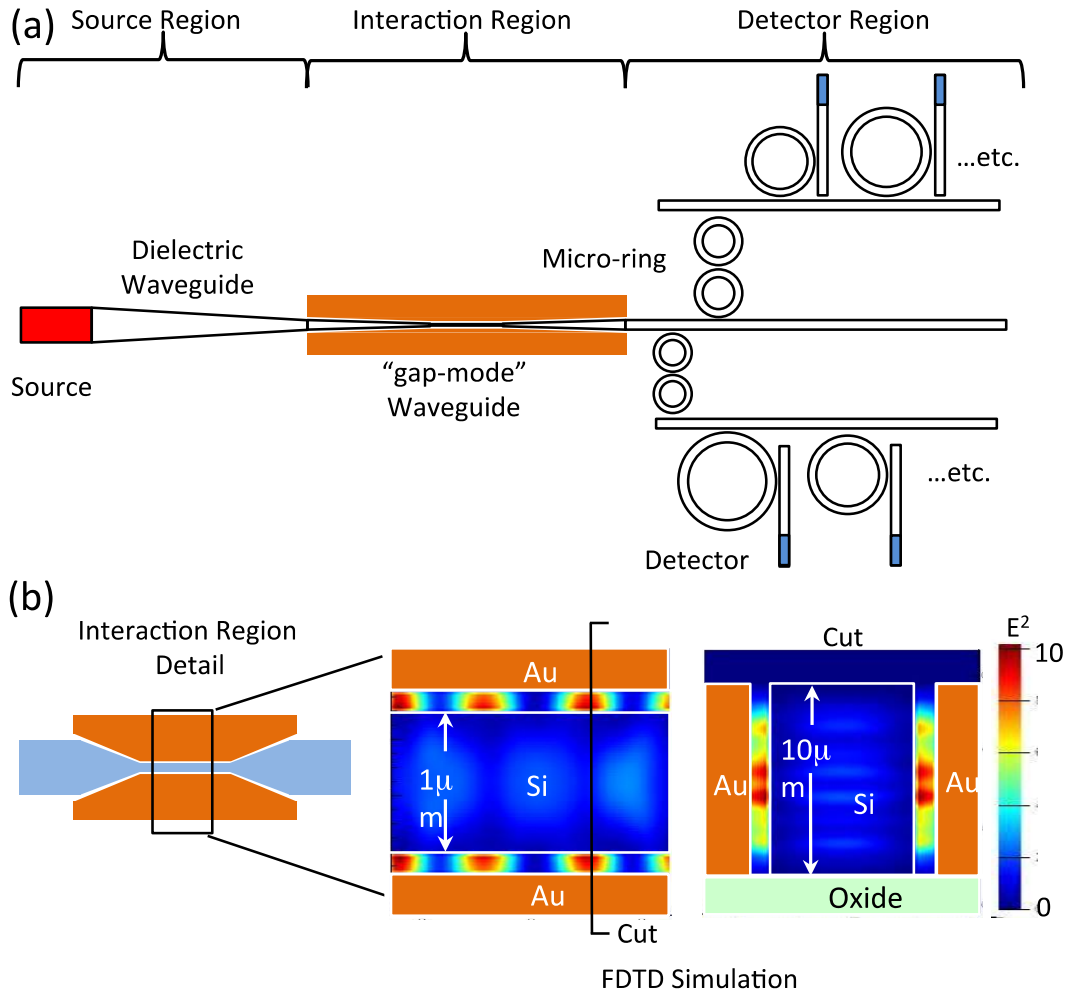
Figure 47(a) Schematic of planar integrated plasmonic mid-IR spectrometer. A broad band LED source feeds a plasmonic based interaction region. The layered micro-ring resonator section as described in the text determines spectral content. (b) FDTD simulation of the interaction region showing generation of plasmon modes in the gap located between the dielectric and the surrounding metal.

Micro-rings resonate when the round trip path length of the optical field is an integral multiple of the effective wavelength of the optical field [4]. The separation between resonances, or the free spectral range, FSR, is inversely proportional to the round trip path length, while the full width half max, FWHM, of any resonance is proportional to the FSR. Decreasing the resonant line width by increasing the round trip path length correspondingly reduces the FSR. Attempts to

increase resolution by decreasing the FWHM of the filter resonance introduce ambiguities in wavelength determination if the excitation bandwidth exceeds the FSR.

To alleviate this problem, a layered micro-ring resonator approach is proposed as it was discussed earlier (Figure 47 (a)). The first layer of filters has a small optical path and its FSR needs only to exceed the LED bandwidth. The second layer of filters has a larger optical path length with a reduced FSR that only needs to be as wide as the first layer's FWHM. This second layer will have a correspondingly smaller FWHM and provides the resolution needed for chemical identification. Unambiguous determination of spectral content results can be achieved by this method.

Silicon waveguides on oxide have been fabricated by DRIE with fluorine chemistry using photolithographically defined metal masks. Figure 48 presents a SEM image of some our waveguides, showing the progression in quality as process development was undertaken. Vertical sidewalls as well as smooth etched surfaces were achieved.
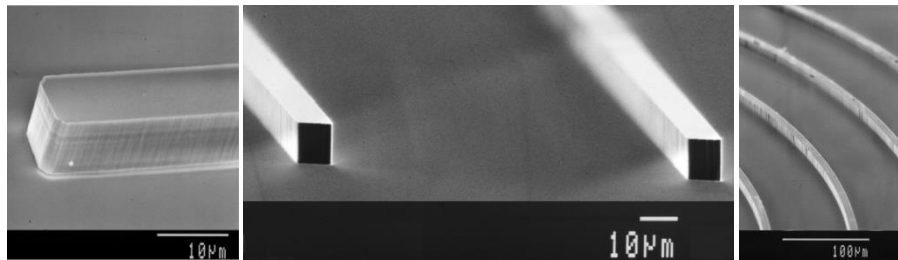
Figure 48 (left) Si waveguide on insulator, (center) Two adjacent Si waveguides 100 μm apart, (right) Bent Si waveguides with different radii of curvature.

6.5 Interaction region

Figure 49 presents our process for patterning the interaction region. Electron-beam lithography is followed by metal evaporation and lift-off to form an etch mask (a). The Si top layer is etched using DRIE, leaving the waveguide structure on top of the oxide layer. A seed layer of ~50 nm of Au is then deposited over the entire area (b), followed by a CVD layer of nitride (c). Conformal coating on the waveguide sidewalls defines the eventual width of the plasmon slot waveguide.

Next, the surface is spin-coated with a thick layer of photoresist and a rectangular window opened by lithography (d). The thickness of this resist layer matches or exceeds the height of the waveguide (10 μm). The nitride is etched by anisotropic RIE (e) to remove Nitride from the horizontal surfaces without removing nitride from the vertical sidewalls. This step is followed by electroplating 10 μm of Au over the window (f). The electrical isolation of the waveguide from the rest of the structure in the window should prevent plating of the top of the waveguide. We then strip the resist (g) and wet etch the Nitride from the sidewalls (h). The thin seed layer of Au is then removed and we are left with the tapered interaction region waveguide separated from the metal plasmon host by a gap of the proper width (i).

FDTD simulations of the interaction region are show in Figure 49 (b). The cross section is a top down view of the waveguide in the interaction region. As the lateral dimension is tapered to a width of 1 μm, the waveguide becomes too narrow to support a waveguided photonic mode, so the electromagnetic energy is forced into the gap where it excites a SPP bound to the metal. The cross section view displayed in the lower right hand corner is a head on view in the propagation direction through the waveguide.
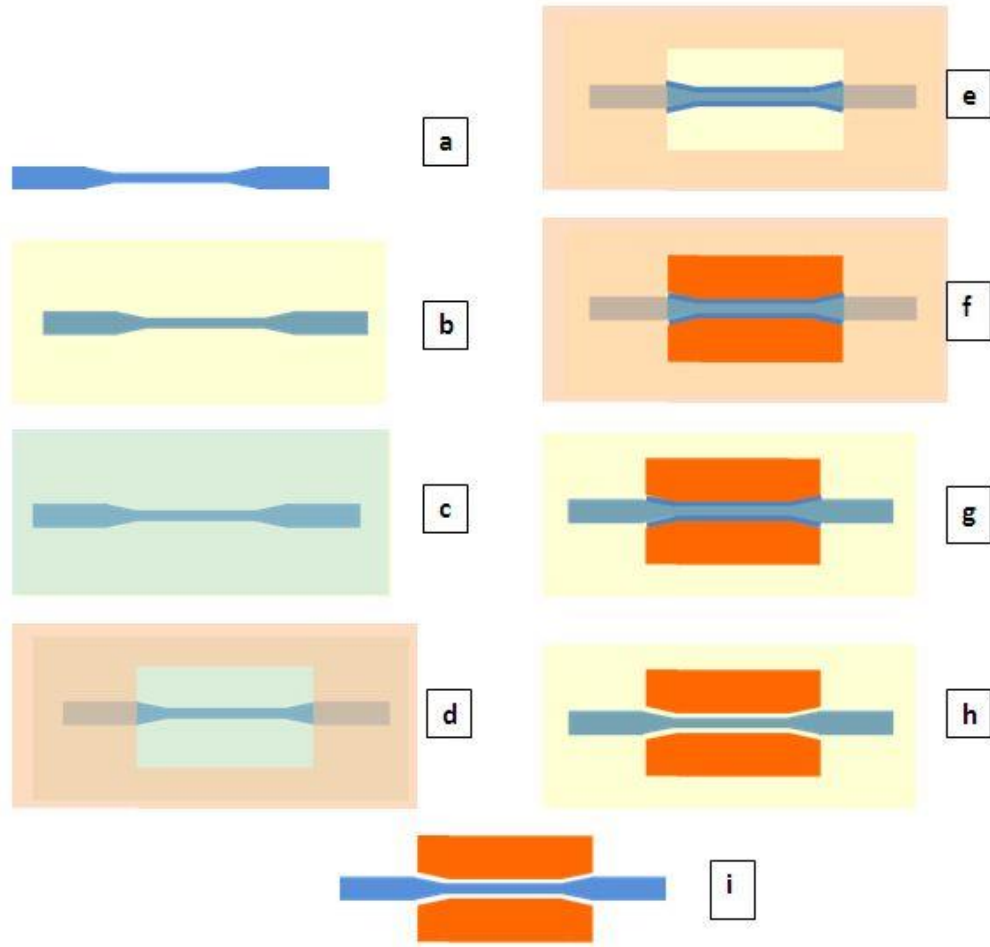
Figure 49 (a-i) Processing steps for fabrication of the interaction region.

An estimate for the necessary length of the interaction region may be obtained by simulating the effect of changing the index in the slot. The relevant parameters are the refractive index, the thickness of the layer, and the extinction coefficient. Alternatively, we may estimate the ratio of transmitted optical intensity, I, to source intensity, I_o, as function of length of using the Beer-Lambert law,

$$\frac{I}{I_o} = T = \exp(-\sigma \, \mathrm{N} x)$$

where σ is the absorption cross section, N is the number per unit volume of absorbing particles. Small ligands ($<$ 300 Da) can have characteristic lengths on the order of 10 Angstrom, while 60 kDa biomolecules can be 10's of nm in length. The diameter of the DNA double helix is roughly 2 nm, but of course the length is orders of magnitude larger. Taking as an example a molecule of 10 nm radius gives a molecular volume of 10^{-18} cm^3, or for 100% concentration, 10^{18} molecules per cm^3.

Estimating an absorption cross section of 10^{-18} cm^2 gives $T = e^{-\sigma x}$. Thus, for an easily measureable change in transmittance due to molecular absorption of 10%, $x = -\ln(0.9) = 1$ mm is obtained suggesting an appropriate interaction region length of 1 mm. The propagation length of surface plasmons on gold at 3 micron wavelength is several millimeters [6]. So, sufficient throughput and sufficient path length for sensing are simultaneously feasible. Figure 50 represents the characteristics SPP propagation lengths of some Si based materials versus Au.
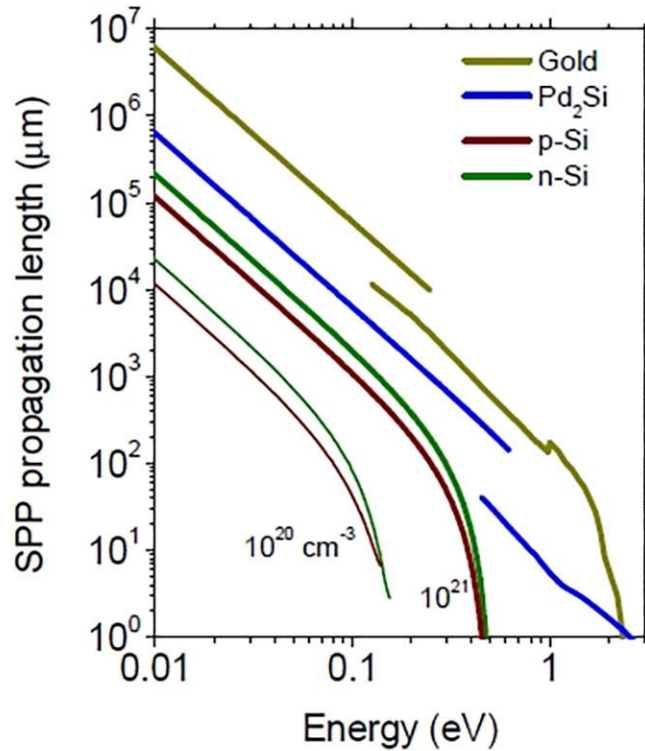
Figure 50 SPP characteristic lengths of p- and n- doped Si, Pd$_2$Si versus Au.

The particular micro-ring resonator of Figure 46 was defined using optical lithography. The corners have radius 3 μm and the 3 μm wide extended straight sections are designed to improve coupling with the waveguides by providing a longer interaction length. The micro-ring resonators to be defined by e-beam lithography will have widths of approximately 1 μm, with distinct channels defined by differences in diameter of tens of nanometers.

As an example, a first layer of micro-ring resonators with 1.58 μm diameters might be used with a second layer of 15.82 μm diameters, where there resonance FWHM of roughly 3 nm would be suitable for chemical identification in the SWIR as proposed. All dimension are well with the range of ebeam lithography and are approaching dimensions whereby optical lithography could be used throughout for the fabrication of this integrated nanophotonic chip.

79

CHAPTER SEVEN: PLASMONIC PHOTOCAPACITOR BASED ON KRETSCHMANN PRISM COUPLER FOR SPECTRAL IMAGING

7.1 Introduction

Hyperspectral imaging systems have been the subject of research for the past two decades [86]. Spectral imaging systems could obtain the spectrum of each pixel in the image of a scene and are extremely useful in earth sciences, chemical identification and remote sensing [87, 88]. Most of commonly used spectral imagers are bulky and possess complicated optics with large moving parts, which makes them expensive to operate in space-based spectral sensing. The opportunity we are looking for here is a plasmonic device that can be potentially used as a spectral imager, in which spectra is obtained by a novel kind of filtering based on a resonant transduction to a detectable SPP.

In this chapter, we will discuss a plasmonic device based on electronic detection of surface plasmon polaritons in a Kretschmann-based prism coupler. Such a device then will be coupled to a photocapacitor while the evanescent field bound to surface plasmon polaritons can penetrate through the air, and can be potentially used for detection applications.

As it was shown earlier in this dissertation, at a specific angle of incidence, the in-plane (TM) part of the incident light can match the momentum of the SPP at a specific optical frequency. For an optimized metal thickness, the incident p-polarized light can be completely converted to SPPs. Consequently, the reflectance from such a device is zero at resonance angle as it is shown in Figure 51 where the light is assumed to be p-polarized and the wavelength is 651 nm.
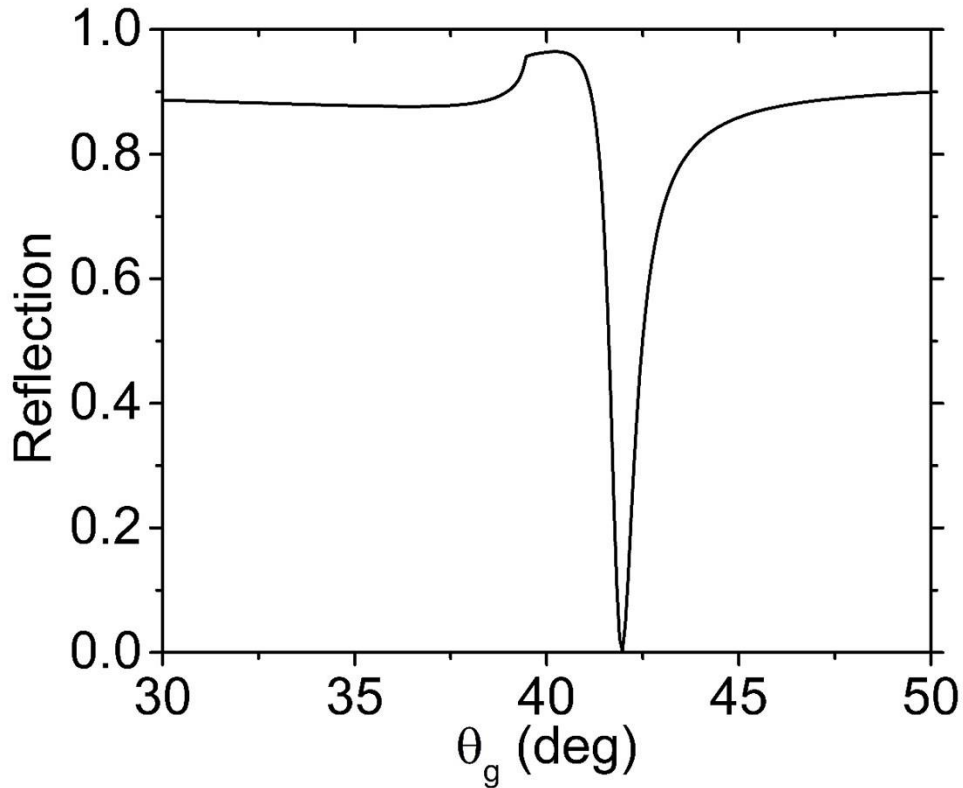
Figure 51 Angular refletnace of a 45 nm thick-Ag evapoarted on a BK7 prsim at 651 nm.

7.2 Plasmonic photocapacitor

The device is based on a Kretschmann prism-coupler that can be potentially used in a special configuration to detect the SPPs electronically. Prism coupler consists of a right-angle BK7 prism with a thin layer of plasmonic metal, in this case Ag, is evaporated by e-beam deposition. As it was shown earlier in this dissertation, SPP can be generated at the interface of Ag/air if a TM polarized light hits on the surface of the metal.

Second part of the device consists of a capacitor that is formed on a lightly p-doped Si (100) substrate with 280 nm of SiO_2 electron beam evaporated on its surface. A very thin layer of a transparent conductor (TC) is deposited on a top of this heterostructures and it will be used to

allow the biasing of the capacitor. Then, Au/Cr contact on sides of the prism can be defined photolithographically on each end of the Au layer of prism and later could be wire-bonded to the Si substrate with Aluminum wires. So, the second part of the device which is a photo-capacitor comprises a silicon substrate, a layer of silicon oxide, and a transparent conductor. The latter may be a thin evaporated metal such as Au, or a transparent conducting oxide such as SnO_2:F, discussed earlier in this dissertation.

The metallic surface of a prism then is mounted on a capacitor with an air gap of 600 nm using SiO_2 standoffs. This standoff is necessary to make the air gap, so SPP will penetrate through photocapacitor and produces the necessary index contrast for SPP excitation at the interface. Transient charging of the Si/SiO_2 interface induces a current in the transparent conductor (i.e., thin Au layer) which passes through the Au/Cr contact to an inverting current amplifier and can be detected. Figure 52 shows the schematic of the proposed device.
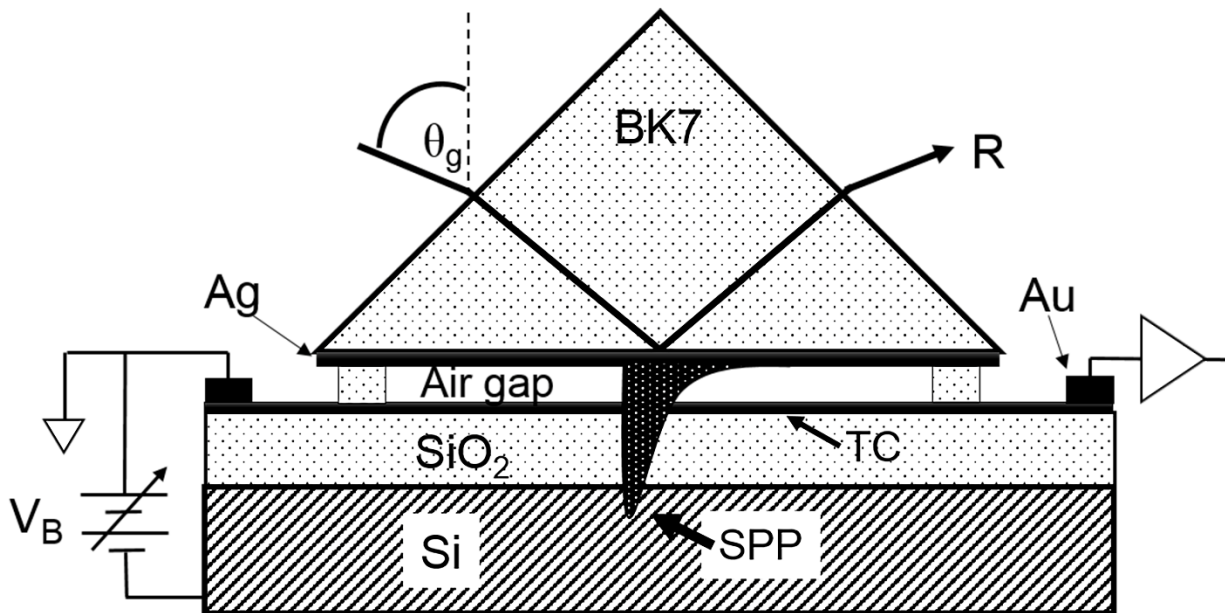
Figure 52 Schematic of a plasmonic photocapacitor.

Exposure to light only at the SPP resonance wavelength and angle of incidence generates electron-hole pairs in the semiconductor. The electrons accumulate at the semiconductor-oxide interface, inducing a current in the transparent conductor, which could be amplified and recorded. Biasing the transparent conductor enables electronic modulation of the photoresponse.

7.3 Optical characterization of the prism-based device in a goniometer setup

For the start, the measured reflectance from a right-angle BK7 prism coated with 45 nm of Ag is shown in Figure 53 for a TM-polarized light at 651 nm. Angular reflectance of the device was then measured in a goniometer setup with a LabView-controlled system. A detector rotates at $2\theta_g$ to synchronously monitor the reflected intensity, and the size of the detector element gives an angular uncertainty of about 0.3 deg. The incident medium was on a BK7 glass, followed by Ag, air, and SiO_2 layers, and the exit medium was silicon. Two laser diodes (LDs) at 651 nm and 532 nm were used as light-sources. Angular reflectivity of the device at 651 nm was measured and is depicted in Figure 52. Angular reflectance is also calculated using permittivity values of Ag, Au, SiO_2 and Si from and is proved to have a minimum around 42 deg [89].
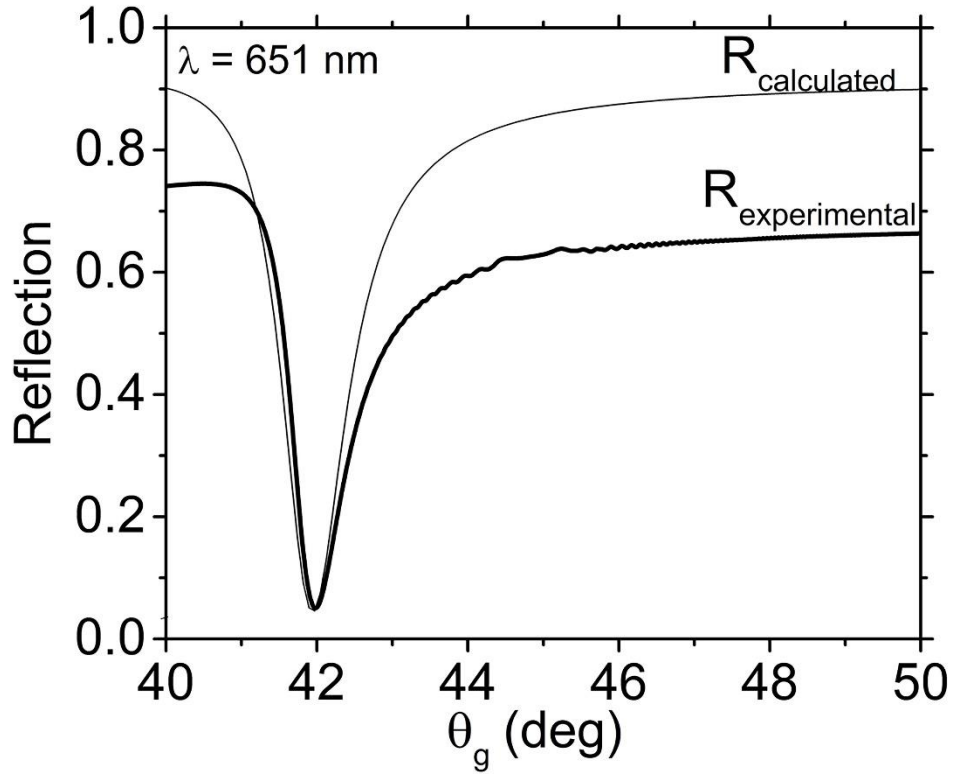
Figure 53 Measured and calculated angular reflection from the device at 651 nm.

The minimum of reflectivity for the TM-polarized light at 532 nm occurs at the resonance angle for excitation of SPPs which is around 43.5 deg. Fresnel calculations for the same structure confirms the prediction of SPP excitation at 43.5 deg for a p-polarized incident light at 532 nm, as it is shown in Figure 54.
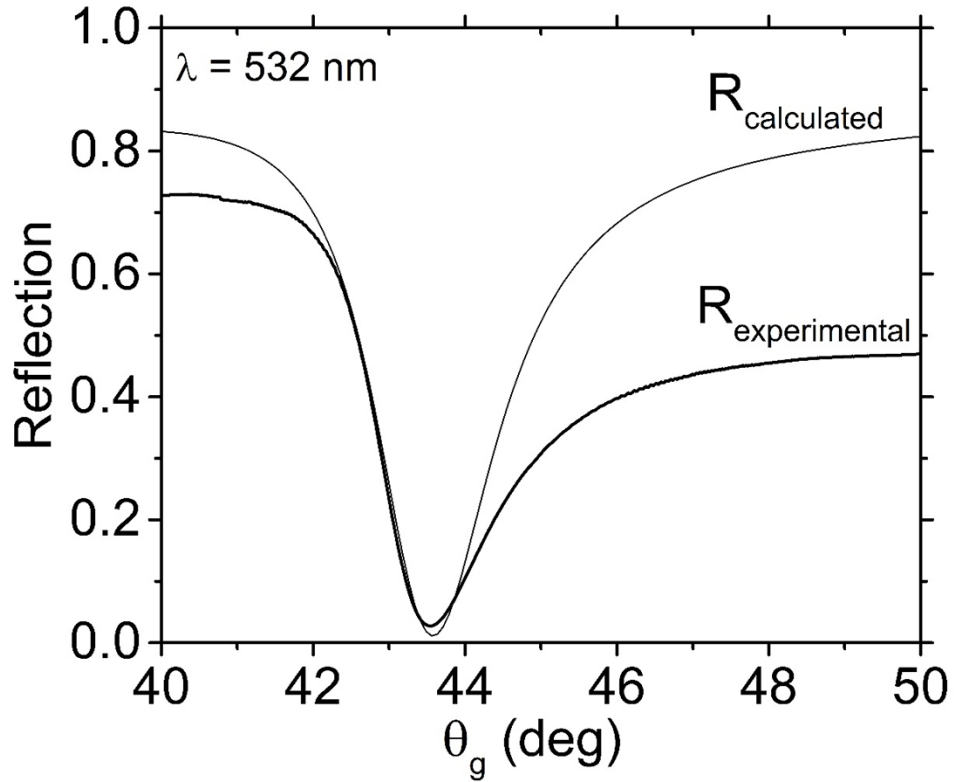
Figure 54 Measured and calculated angular reflection from the device at 532 nm.

Transmission of the device inside the Si can be also acquired by Fresnel calculations. We expect such a transmission to closely match the photo-induced current curve for the device, once it is measured.

CHAPTER EIGHT: CONCLUDING REMARKS

Focus of this work is on the extension of the use of SPPs in mid-infrared range of the spectrum in order to achieve efficient plasmonic devices that can support strong SPP confinement modes with low loss. IR SPP properties are investigated by prism- and grating- couplers for variety of novel hosts such as semimetals and doped semiconductors.

Optically thick bismuth films were fabricated by electron beam and thermal evaporation methods and their optical characteristics were investigated by means of scanning electron microscopy, x-ray diffraction and ellipsometry. Permittivity spectra of bismuth films in range of 1.4 to 40 microns were measured and compared to earlier published reports. Bismuth lamellar gratings were also fabricated by photolithography and evaporation techniques. Resonances of bismuth lamellar gratings in range of 8 to 10.5 microns were observed and studied. These extinction resonances can be useful in sensing applications in infrared. Therefore, bismuth with plasma frequency of two orders of magnitude smaller than traditional noble metals, could be potentially used in mid- to long-wave IR devices.

In recent years, lot of attention has been shifted to several transparent conducting oxides (TCOs), such as indium tin oxide (ITO) and aluminum doped zinc oxide (AZO), for their promising plasmonic properties. TCO have already been used in verity of opto-electronic devices although they have a lower carrier concentration (10^{20-22} cm^{-3}) comparing to noble metals (10^{23} cm^{-3}). Consequently, TCOs possess lower plasma frequencies in infrared wavelength which makes them a candidate for applications in IR plasmonics.

We have developed a CMOS compatible and highly useful transparent conducting thin-films of SnO_2: F which were grown on preheated glass and silicon substrate, by Streaming Process for Electrodeless Electrochemical Deposition (SPEED). SPEED allows high-quality film growth on large area hydrophilic rigid or flexible substrates, at lower temperature than the traditional spray pyrolysis, using environmentally friendly water-soluble primary chemicals and very flexible chemistry formulation for binary or more complex compound materials growth. Stannic chloride ($SnCl_4$) and ammonium fluoride (NH_4F) dissolved in a mixture of deionized water and organic solvents were used as precursors. The preheated substrate temperature was varied between 440 and 500 °C. High quality SnO_2:F films were grown at all the substrate temperatures studied. The resulting typical film thickness was 250 nm. X-ray diffraction shows that the grown films are polycrystalline SnO_2 with a tetragonal crystal structure. The average optical transmission of the films was around 93% throughout the wavelength range 400 to 1000 nm. The lowest electrical resistivity achieved was 6×10^{-4} Ω-cm. The Hall measurements showed that the film is an n-type semiconductor, with carrier mobility of 8.3 cm^2/V-s, and carrier concentration of 1×10^{21} cm^{-3}. The direct bandgap was determined to be 4.0 eV from the transmittance spectrum.

Optical properties of FTO films grown by SPEED were characterized by means of ellipsometry and FTIR reflectance. Si gratings were also fabricated photolithographically and then were etched by (DRIE) in order to produce Si grating with 1.5 micron amplitude and various periods. A thin layer SiO_2 then was deposited onto the Si gratings by plasma enhanced chemical vapor deposition (PECVD) in order to coat the Si grating with a hydrophilic layer and ready for the SPEED deposition of FTO. The deposited FTO coating was found to be uniform across both grating bars and sidewalls. Distinct resonances due to excitation of SPPs were observed in angular- and specular- reflection measurements of FTO gratings in a goniometer setup. Such resonances

could be potentially useful in sensing and design and development of efficient plasmonic devices in the mid-IR range.

In an effort to introduce a novel mid-IR plasmonic device, a compact spectrometer-on-a-chip featuring a plasmonic molecular interaction region was conceived, designed, modeled, and partially fabricated. The silicon-on-insulator (SOI) system was the chosen platform for the integration due to its CMOS compatibility. The low loss of both silicon and SiO_2 between 3 and 4 μm wavelengths enables silicon waveguides on SiO_2 as the basis for molecular sensors at these wavelengths. Important characteristic molecular vibrations occur in this range, namely the bond stretching modes C-H (Alkynes), O-H (monomeric alcohols, phenols) and N-H (Amines), as well as CO double bonds, NH_2, and CN. The device consists of a broad-band infrared LED, photonic waveguides, photon-to-plasmon transformers, a molecular interaction region, dispersive structures, and detectors. Photonic waveguide modes are adiabatically converted into SPPs on a neighboring metal surface by a tapered waveguide. The plasmonic interaction region enhances optical intensity, which allows a reduction of the overall device size without a reduction of the interaction length, in comparison to ordinary optical methods. After the SPPs propagate through the interaction region, they are converted back into photonic waveguide modes by a second taper. The dispersing region consists of a series of micro-ring resonators with photodetectors coupled to each resonator. Design parameters were optimized via electro-dynamic simulations. Fabrication was performed using a combination of photo- and electron-beam-lithography together with standard silicon processing techniques.

Optical properties of a plasmonic photocapacitor based on a Kretschmann prism-coupler that can be potentially useful in spectral imaging was also investigated. A TM-polarized laser light at 651 and 532 nm wavelength was electronically chopped at 1 kHz while the beam was internally

88

reflected from the metalized prism face. The angle of incidence relative to goniometer, θ_g was varied by a motor controlled goniometer with a photodetector which rotated at $2\theta_g$ to synchronously monitor the reflected intensity. Fresnel equations were used to calculate the reflectivity spectra of this Kretschmann-based prism device. The excitation of SPPs at both wavelengths were confirmed by these calculations.

APPENDIX: PUBLICATIONS

Journal publications:

1. Farnood Khalilzadeh-Rezaie et al., **"Transparent conductor-silicon plasmonic photocapicitor for spectral imaging,"** *J. Appl. Phys.* (In preparation).

2. Farnood Khalilzadeh-Rezaie et al., **"Plasmonic properties of fluorine-doped tin oxide thin films in the near-infrared,"** *Opt. Mater. Exp.* (Under review).

3. Janardan Nath, Shushrut Modak, Imen Rezadad, Deep Panjwani, Farnood Khalilzadeh-Rezaie, and Robert E. Peale, **"Far-infrared absorber based on standing-wave resonances in metal-dielectric cavity,"** *Opt. Exp.* (In press).

4. Farnood Khalilzadeh-Rezaie et al., "**Infrared surface polaritons on bismuth,"** *J. Nanophoton.* 9(1), 093792 (2015).

5. Gaungming Tao, Soroush Shabahang, He Ren, Farnood-Khalilzadeh-Rezaie et al., **"Robust metamaterial tellurium-based chalcogenide glass fibers for mid-wave and long-wave infrared transmission,"** *Opt. Lett.* 39 (13), 4009-4012 (2014).

Conference proceedings:

1. Farnood Khalilzadeh-Rezaie et al., **"Metal-oxide-semiconductor plasmonic photocapicitor for sensing surface plasmon polaritons,"** *SPIE Optical Engineering+ Applications (OP15O)*, (accepted).

2. Janardan Nath, Deep Panjwani, Mehmet Yesiltas, Farnood Khalilzadeh-Rezaie et al., "**Synchrotron infra-red spectroscopy of metal-dielectric-metal cavity metamaterial absorbers,"** *SPIE NanoScience +Engineering (OP15N)*, (accepted).

3. Farnood Khalilzadeh-Rezaie et al., **"Optical and electrical properties of tin based transparent conducting oxides,"** *Proc. MRS* **1805** (2015).

4. Guangming Tao, Soroush Shabahang, He Ren, <u>Farnood Khalilzadeh-Rezaie</u> et al., **"Robust multimaterial tellurium-based chalcogenide glass infrared fibers,"** *CLEO*: Science and Innovations (2014).

5. <u>Farnood K. Rezaie</u> et al., **"Junctionless thin-film ferroelectric oxides Ferroelectric oxides for photovoltaic energy production,"** *Proc. SPIE* **9115** 27 (2014).

6. <u>Farnood K. Rezaie</u> et al., **"Planar integrated Mid IR spectrometer,"** *Proc. MRS* **7680** (2012).

7. C. J. Fredricksen, Justin W. Cleary, Walter R. Buchwald, Pedro Figueiredo, <u>Farnnod Khalilzdeh-Rezaie</u> et al., **"Planar integrated plasmonic Mid-IR spectrometer,"** *Proc. SPIE* **835321** (2011).

LIST OF REFERENCES

1. Wood, R.W., *On a remarkable case of uneven distribution of light in a diffraction grating spectrum.* 1902.

2. Rayleigh, L., *On the dynamical theory of gratings.* Proceedings of the Royal Society of London. Series A, Containing Papers of a Mathematical and Physical Character, 1907. **79**(532): p. 399-416.

3. Fano, U., *The theory of anomalous diffraction gratings and of quasi-stationary waves on metallic surfaces (Sommerfeld's waves).* JOSA, 1941. **31**(3): p. 213-222.

4. Bohm, D. and D. Pines, *A collective description of electron interactions: III. Coulomb interactions in a degenerate electron gas.* Physical Review, 1953. **92**(3): p. 609.

5. Ritchie, R., *Plasma losses by fast electrons in thin films.* Physical Review, 1957. **106**(5): p. 874.

6. Otto, A., *Excitation of nonradiative surface plasma waves in silver by the method of frustrated total reflection.* Zeitschrift für Physik, 1968. **216**(4): p. 398-410.

7. Kretschmann, E. and H. Raether, *Radiative decay of non radiative surface plasmons excited by light(Surface plasma waves excitation by light and decay into photons applied to nonradiative modes).* Zeitschrift Fuer Naturforschung, Teil A, 1968. **23**: p. 2135.

8. Whittaker, D. and I. Culshaw, *Scattering-matrix treatment of patterned multilayer photonic structures.* Physical Review B, 1999. **60**(4): p. 2610.

9. Liscidini, M., et al., *Scattering-matrix analysis of periodically patterned multilayers with asymmetric unit cells and birefringent media.* Physical Review B, 2008. **77**(3): p. 035324.

10. Brongersma, M.L. and P.G. Kik, *Surface plasmon nanophotonics*. 2007: Springer.

11.   Maier, S.A., *Plasmonics: fundamentals and applications: fundamentals and applications*. 2007: Springer Science & Business Media.

12.   Sarid, D. and W. Challener, *Modern introduction to surface plasmons: theory, Mathematica modeling, and applications*. 2010: Cambridge University Press.

13.   Liedberg, B., C. Nylander, and I. Lunström, *Surface plasmon resonance for gas detection and biosensing*. Sensors and actuators, 1983. **4**: p. 299-304.

14.   Nylander, C., B. Liedberg, and T. Lind, *Gas detection by means of surface plasmon resonance*. Sensors and Actuators, 1983. **3**: p. 79-88.

15.   Schasfoort, R.B. and A.J. Tudos, *Handbook of surface plasmon resonance*. 2008: Royal Society of Chemistry.

16.   Markey, F., *Principles of surface plasmon resonance*, in *Real-Time Analysis of Biomolecular Interactions*. 2000, Springer. p. 13-22.

17.   Homola, J., S.S. Yee, and G. Gauglitz, *Surface plasmon resonance sensors: review*. Sensors and Actuators B: Chemical, 1999. **54**(1): p. 3-15.

18.   Jönsson, U., et al., *Real-time biospecific interaction analysis using surface plasmon resonance and a sensor chip technology*. Biotechniques, 1991. **11**(5): p. 620-627.

19.   Soref, R.A. and J.P. Lorenzo, *All-silicon active and passive guided-wave components for lambda= 1.3 and 1.6 microns*. IEEE Journal of Quantum Electronics, 1986. **22**: p. 873-879.

20.   Soref, R., *The past, present, and future of silicon photonics*. Selected Topics in Quantum Electronics, IEEE Journal of, 2006. **12**(6): p. 1678-1687.

21.   Soref, R., *Silicon photonics: a review of recent literature*. Silicon, 2010. **2**(1): p. 1-6.

22.   Soref, R., *Mid-infrared photonics in silicon and germanium.* Nature Photonics, 2010. **4**(8): p. 495-497.

23.   Murray, W.A. and W.L. Barnes, *Plasmonic materials.* Advanced materials, 2007. **19**(22): p. 3771-3782.

24.   Dionne, J.A. and H.A. Atwater, *Plasmonics: Metal-worthy methods and materials in nanophotonics.* MRS Bulletin, 2012. **37**(08): p. 717-724.

25.   Stanley, R., *Plasmonics in the mid-infrared.* Nature Photonics, 2012. **6**(7): p. 409-411.

26.   Shahzad, M., et al., *Infrared surface plasmons on heavily doped silicon.* Journal of Applied Physics, 2011. **110**(12): p. 123105.

27.   Cleary, J.W., et al., *Infrared surface polaritons on antimony.* Optics express, 2012. **20**(3): p. 2693-2705.

28.   Noginov, M., et al., *Transparent conductive oxides: Plasmonic materials for telecom wavelengths.* Applied Physics Letters, 2011. **99**(2): p. 021101.

29.   Zhong, Y., et al., *Review of mid-infrared plasmonic materials.* Journal of Nanophotonics, 2015. **9**(1): p. 093791-093791.

30.   Cleary, J.W., et al., *Platinum germanides for mid- and long-wave infrared plasmonics.* optics express, 2015: p. in press.

31.   Landau, L.D., et al., *Electrodynamics of continuous media*. Vol. 8. 1984: Elsevier.

32.   Ordal, M., et al., *Optical properties of the metals al, co, cu, au, fe, pb, ni, pd, pt, ag, ti, and w in the infrared and far infrared.* Applied Optics, 1983. **22**(7): p. 1099-1119.

33.   Seymour, R., J. Krupczak Jr, and G. Stegeman, *High efficiency coupling to the overcoated surface plasmon mode in the far infrared.* Applied Physics Letters, 1984. **44**(4): p. 373-375.

34.   Homola, J., *Present and future of surface plasmon resonance biosensors.* Analytical and bioanalytical chemistry, 2003. **377**(3): p. 528-539.

35.   Tediosi, R., et al., *Charge carrier interaction with a purely electronic collective mode: Plasmarons and the infrared response of elemental bismuth.* Physical review letters, 2007. **99**(1): p. 016406.

36.   Shahzad, M., *Infrared Surface Plasmon Polaritons on Semiconductor, Semimetal and Conducting Polymer.* 2012, University of Central Florida Orlando, Florida.

37.   Shahzad, M., et al. *Infrared surface waves on semiconductor and conducting polymer.* in *SPIE Defense, Security, and Sensing.* 2011. International Society for Optics and Photonics.

38.   Tompkins, H. and E.A. Irene, *Handbook of ellipsometry.* 2005: William Andrew.

39.   Hodgson, J., *The infra-red properties of Bismuth.* Proceedings of the Physical Society. Section B, 1954. **67**(3): p. 269.

40.   Lenham, A., D. Treherne, and R. Metcalfe, *Optical properties of antimony and bismuth crystals.* JOSA, 1965. **55**(9): p. 1072-1074.

41.   Hoffman, C., et al., *Semimetal-to-semiconductor transition in bismuth thin films.* Physical Review B, 1993. **48**(15): p. 11431.

42.   Ginley, D.S. and C. Bright, *Transparent Conducting Oxides.* MRS Bulletin, 2000. **25**(08): p. 15-18.

43.   Coutts, T.J., et al., *Transparent conducting oxides: status and opportunities in basic research.* Proc. Electrochem. Soc, 1999. **99**(1999): p. 274-288.

44.   Fortunato, E., et al., *Transparent conducting oxides for photovoltaics.* Mrs Bulletin, 2007. **32**(03): p. 242-247.

45. Stadler, A., *Transparent conducting oxides—An up-to-date overview.* Materials, 2012. **5**(4): p. 661-683.

46. Liu, H., et al., *Transparent conducting oxides for electrode applications in light emitting and absorbing devices.* Superlattices and Microstructures, 2010. **48**(5): p. 458-484.

47. Wang, Y., et al., *Mesostructured SnO2 as sensing material for gas sensors.* Solid-State Electronics, 2004. **48**(5): p. 627-632.

48. Batzill, M., et al., *Tuning the chemical functionality of a gas sensitive material: Water adsorption on SnO< sub> 2</sub>(101).* Surface science, 2006. **600**(4): p. 29-32.

49. Amma, D., V. Vaidyan, and P. Manoj, *Structural, electrical and optical studies on chemically deposited tin oxide films from inorganic precursors.* Materials chemistry and physics, 2005. **93**(1): p. 194-201.

50. Martyla, A., et al., *Platinum (0)-1, 3-divinyl-1, 1, 3, 3-tetramethyldisiloxane Complex as a Pt Source for Pt/SnO 2 Catalyst.* Journal of Nanomaterials, 2014. **2014**.

51. Mario A, S.-G., et al., *Characteristics of SnO 2: F Thin Films Deposited by Ultrasonic Spray Pyrolysis: Effect of Water Content in Solution and Substrate Temperature.* Materials Sciences and Applications, 2012. **2012**.

52. Rakhshani, A., Y. Makdisi, and H. Ramazaniyan, *Electronic and optical properties of fluorine-doped tin oxide films.* Journal of Applied Physics, 1998. **83**(2): p. 1049-1057.

53. Leja, E., T. Pisarkiewicz, and A. Kołodziej, *Electrical properties of non-stoichiometric tin oxide films obtained by the dc reactive sputtering method.* Thin Solid Films, 1980. **67**(1): p. 45-48.

54.   Elangovan, E. and K. Ramamurthi, *Studies on micro-structural and electrical properties of spray-deposited fluorine-doped tin oxide thin films from low-cost precursor.* Thin solid films, 2005. **476**(2): p. 231-236.

55.   Sujatha, C., G.M. Rao, and S. Uthanna, *Characteristics of indium tin oxide films deposited by bias magnetron sputtering.* Materials Science and Engineering: B, 2002. **94**(1): p. 106-110.

56.   Onuma, Y., et al., *Preparation and piezoresistive properties of polycrystalline SnO2 films.* Japanese journal of applied physics, 1998. **37**(3R): p. 963.

57.   Homma, H., et al., *SnO2 grazing-incidence antireflection films for monochromatization of synchrotron radiation: Design, preparation, and characterization.* Journal of applied physics, 1992. **72**(12): p. 5668-5675.

58.   Aboaf, J., V. Marcotte, and N. Chou, *Chemical composition and electrical properties of tin oxide films prepared by vapor deposition.* Journal of The Electrochemical Society, 1973. **120**(5): p. 701-702.

59.   Huaman, J.L.C., et al., *Copper nanoparticles synthesized by hydroxyl ion assisted alcohol reduction for conducting ink.* Journal of Materials Chemistry, 2011. **21**(20): p. 7062-7069.

60.   Oladeji, I.O., *Film growth system and method.* 2010, US Patent.

61.   Oladeji, I.O., *Method for fabricating copper-containing ternary and quaternary chalcogenide thin films.* 2011, US Patent.

62.   Rezaie, F.K., et al. *Junctionless thin-film ferroelectric oxides for photovoltaic energy production.* in *SPIE Sensing Technology+ Applications.* 2014. International Society for Optics and Photonics.

63. Oladeji, I.O. and L. Chow, *Optimization of chemical bath deposited cadmium sulfide thin films.* Journal of the Electrochemical Society, 1997. **144**(7): p. 2342-2346.

64. Varghese, O.K., L. Malhotra, and G. Sharma, *High ethanol sensitivity in sol–gel derived SnO< sub> 2</sub> thin films.* Sensors and Actuators B: Chemical, 1999. **55**(2): p. 161-165.

65. Miao, D., et al., *Effect of substrate temperature on the crystal growth orientation of SnO< sub> 2</sub>: F thin films spray-deposited on glass substrates.* Journal of Non-Crystalline Solids, 2010. **356**(44): p. 2557-2561.

66. Agashe, C. and S. Mahamuni, *Competitive effects of film thickness and growth rate in spray pyrolytically deposited fluorine-doped tin dioxide films.* Thin Solid Films, 2010. **518**(17): p. 4868-4873.

67. Riveros, R., E. Romero, and G. Gordillo, *Synthesis and characterization of highly transparent and conductive SnO2: F and In2O3: Sn thin films deposited by spray pyrolysis.* Brazilian Journal of Physics, 2006. **36**(3B): p. 1042-1045.

68. Smith, A., et al., *Relation between solution chemistry and morphology of SnO< sub> 2</sub>-based thin films deposited by a pyrosol process.* Thin Solid Films, 1995. **266**(1): p. 20-30.

69. Elangovan, E. and K. Ramamurthi, *Optoelectronic properties of spray deposited SnO 2: F thin films for window materials in solar cells.* Journal of Optoelectronics and Advanced Materials, 2003. **5**(1): p. 45-54.

70. Haitjema, H., J. Elich, and C. Hoogendoorn, *The optical, electrical and structural properties of fluorine-doped, pyrolytically sprayed tindioxide coatings.* Solar energy materials, 1989. **18**(5): p. 283-297.

71.   Aouaj, M.A., et al., *Comparative study of ITO and FTO thin films grown by spray pyrolysis.* Materials Research Bulletin, 2009. **44**(7): p. 1458-1461.

72.   Pommier, R., C. Gril, and J. Marucchi, *Sprayed films of indium tin oxide and fluorine-doped tin oxide of large surface area.* Thin Solid Films, 1981. **77**(1–3): p. 91-98.

73.   Gordillo, G., et al., *Preparation and characterization of SnO2 thin films deposited by spray pyrolysis from SnCl2 and SnCl4 precursors.* Thin Solid Films, 1994. **252**(1): p. 61-66.

74.   Moss, T.S., *Optical properties of semi-conductors*. 1959, London: Butterworths.

75.   Haacke, G., *New figure of merit for transparent conductors.* Journal of Applied Physics, 1976. **47**(9): p. 4086-4089.

76.   West, P.R., et al., *Searching for better plasmonic materials.* Laser & Photonics Reviews, 2010. **4**(6): p. 795-808.

77.   Feigenbaum, E., K. Diest, and H.A. Atwater, *Unity-order index change in transparent conducting oxides at visible frequencies.* Nano letters, 2010. **10**(6): p. 2111-2116.

78.   Brewer, S.H. and S. Franzen, *Optical properties of indium tin oxide and fluorine-doped tin oxide surfaces: correlation of reflectivity, skin depth, and plasmon frequency with conductivity.* Journal of alloys and compounds, 2002. **338**(1): p. 73-79.

79.   Brewer, S.H., et al., *Investigation of the electrical and optical properties of iridium oxide by reflectance FTIR spectroscopy and density functional theory calculations.* Chemical physics, 2005. **313**(1): p. 25-31.

80.   Franzen, S., et al., *Plasmonic phenomena in indium tin oxide and ITO-Au hybrid films.* Optics letters, 2009. **34**(18): p. 2867-2869.

81.   Dominici, L., et al., *Plasmon polaritons in the near infrared on fluorine doped tin oxide films.* Optics express, 2009. **17**(12): p. 10155-10167.

82. Soref, R., R.E. Peale, and W. Buchwald, *Longwave plasmonics on doped silicon and silicides.* Optics express, 2008. **16**(9): p. 6507-6514.

83. Feng, N.-N. and L. Dal Negro, *Plasmon mode transformation in modulated-index metal-dielectric slot waveguides.* Optics letters, 2007. **32**(21): p. 3086-3088.

84. Mashanovich, G.Z., et al., *Low loss silicon waveguides for the mid-infrared.* Optics Express, 2011. **19**(8): p. 7112-7119.

85. Soref, R.A., J. Schmidtchen, and K. Petermann, *Large single-mode rib waveguides in GeSi-Si and Si-on-SiO 2.* Quantum Electronics, IEEE Journal of, 1991. **27**(8): p. 1971-1974.

86. Chang, C.-I., *Hyperspectral imaging: techniques for spectral detection and classification*. Vol. 1. 2003: Springer Science & Business Media.

87. Adams, J.B. and A.R. Gillespie, *Remote sensing of landscapes with spectral images: A physical modeling approach*. 2006: Cambridge University Press.

88. Pieters, C.M. and P.A. Englert, *Remote geochemical analysis, elemental and mineralogical composition*. Vol. 1. 1993.

89. Palik, E.D., *Handbook of optical constants of solids*. Vol. 3. 1998: Academic press.